Tunable Piezoelectric Transducers via Custom 3D Printing: Conceptualization, Creation, and Customer Discovery of Acoustic Applications

Dominic E LoPinto

Thesis submitted to the faculty of the Virginia Polytechnic Institute and State University
in partial fulfillment of the requirements for the degree of

Master of Science
In
Mechanical Engineering

Xiaoyu (Rayne) Zheng, Chair
Alexander Leonessa, Co-Chair
Eli Vlaisavljevich
Shima Shahab

May 4, 2021
Blacksburg, Virginia

Keywords: piezoelectrics, transducer, metamaterials, beam pattern, stereolithography architected lattice, customer discovery

Tunable Piezoelectric Transducers via Custom 3D Printing: Conceptualization, Creation, and Customer Discovery of Acoustic Applications

Dominic E. LoPinto

ABSTRACT

In an increasingly data-driven society, sensors and actuators are the bridge between the physical world and the world of "data." Electroacoustic transducers convert acoustic energy into electrical energy (or vice versa), so it can be interpreted as data. Piezoelectric materials are often used for transducer manufacturing, and recent advancements in additive manufacturing have enabled this material to take on complex geometric forms with micro-scale features. This work advances the additive manufacturing of piezoelectric materials by developing a model for predictive success of complex 3D printed geometries in Mask Image Projection-Stereolithography (MIP-SL) by accounting for mechanical wear on Polydimethylsiloxane (PDMS). This work proposes a framework for the rapid manufacture of 3D printed transducers, adaptable to a multitude of transducer element forms. Using the print model and transducer framework, latticed hydrophone elements are designed and tested, showing evidence of selectively tunable sensitivity, resonance, and directivity pattern. These technology advancements are extended to enable a workflow for users to input polar coordinates and receive an acoustic element of a continuously tuned directivity pattern. Investigation into customer problem spaces via tech-push methods are adapted from the NSF's Lean Launchpad to reveal insight to the problems faced in hydrophone applications and other neighboring problem spaces.

Development of Tunable Transducers via Custom 3D Printing:
Conceptualizations to Customer Needs

Dominic E. LoPinto

GENERAL AUDIENCE ABSTRACT

In an increasingly data-driven world, sensors are the bridge between the physical world and the world of "data." The better the sensor; the better the data. Electroacoustic transducers are sensors that convert acoustic sound energy into electrical energy or vice versa. These are observed in the world around us as microphones, speakers, ultrasound devices, and more. In the early 1900's, piezoelectric materials became one of the dominant methods for transducer creation, and recent advancements in additive manufacturing have enabled this material to take on highly complex geometric forms with micro-scale feature sizes. Further advancements to additive manufacturing of piezoelectric materials are contributed through development of a model for predicting the success of complex 3D printed geometries in an Mask Image Projection-Stereolithography (MIP-SL) by accounting for mechanical wear on the Polydimethylsiloxane (PDMS) print window. This work proposes a framework for the rapid manufacture of 3D printed transducers, adaptable to a multitude of element forms. Using the developed print model and transducer framework, latticed hydrophone elements are designed and tested, showing evidence of selectively tunable sensitivity, resonance and beampattern. The advancements in technology are extended to enable a workflow for users to input polar coordinates and receive an acoustic element of continuously tuned beampattern. Investigation into customer problem spaces via tech-push methods are adapted from NSF's Lean Launchpad and reveals great insight to the problems faced in hydrophone applications and other neighboring industry spaces.

DEDICATION & ACKNOWLEDGEMENTS

I am grateful for the love and support I have been given from all those: family, friends, mentors and any who fall in-between. Thank you for your endless encouragement, love, and support.

Thank you to Dr. Xiaoyu ‘Rayne’ Zheng, for encouraging me to pursue and explore my passions through the work on this thesis and in the lab. Thank you for your insights, and support of my life’s endeavors, even while separated by 3 time zones of difference.

I would like to thank Dr. Alexander Leonessa for sticking with me from the beginning of my graduate pursuits; I greatly appreciate the doors you have opened and the support you continue to provide from the background as I find my path through interdisciplinary fields of study and experience.

I thank my colleague Huachen Cui for his continued active involvement in this work amid the becoming of a new parent as well as each of my lab mates for their contributions, collaborations, guidance, and friendship.

I would also thank my committee members, Dr. Eli Vlaisavljevichli and Dr. Shima Shahab for their help and valuable insights into technical aspects and potential values of the work I have completed here.

Finally, I thank each of the individuals I have worked with in the CEED community which I have been fortunate to become a part of from day 1on the Virginia Tech campus. Your community support, rich conversations and funding have enabled me to continue to grow at an accelerated pace, expanding my humility, competency, and awareness of the world I am becoming increasingly a part of.

I dedicate this to my dear family, my partner, and my closest friend as you all have been grounding through these unforgettable pandemic years, as a foundation of love and support regardless of all aversions of my path through which I have grown. I dedicate this to all those I encountered in the past two years, each perspective contributing to my path, goals, and accomplishments. I seek to enable a better experience of the world for each of you.

Table of Contents

List of Figures

Chapter 1: Introduction

In an increasingly data-driven world, sensors and actuators are the gatekeepers between the physical world and the digital world [1], [2]. The abilities of these devices limit or enable systems that could only be dreamt of prior [3]. It is not enough, however, to simply develop a technology; to impact the world with it; there must be a meshing of the technology with those who value the benefits it provides[4], [5].

In this work, a novel concept for acoustic sensing is taken through stages of development, from conceptualization to design, manufacture, and customer discovery. Repeatable frameworks and processes are developed throughout each step including a generalized framework for transducer manufacturing, a model for additive manufacturing of highly viscous resins, a repeatable design process to make mass-customization possible, and a method for technology-push customer discovery.

This chapter provides the background knowledge necessary to understand the contents of this thesis, an overview of literature and existing applications which drove the development of the work, and the motivation behind the work. The chapter comes to a close by outlining the structure of the contributions presented within this work.

1.1. Background Fundamentals

Underwater and medical applications of electroacoustic piezoelectric transducer are the focus of this paper. Each of these terms will be explained along with foundational concepts of piezoelectric materials and underwater hydrophones. This section additionally provides a foundation for additive manufacturing, specifically slurry-based stereolithography.

Transducers

"A **transducer** is a process or a device that converts energy from one form to another." [6]. Tier 2 of Figure 1 displays the physical quantities that may be either converted to or from another physical quantity[1]. **Electroacoustic transducers** (referred as just "transducers" henceforth) lie at the conversion to and from electrical effects; they will behave in one of three ways: receive sound and turn it into an electrical signal (receiving transducers such as a microphone), take in an electric signal and output acoustic pressure (transmitting transducers such as speakers), or execute both roles (transducers such as SONAR systems) [7]. These transducers can facilitate this conversion of energy in numerous ways: electrodynamic, electrostatic, electromagnetic, EM induction, Magnetorestrictive and piezoelectric [7], [8].

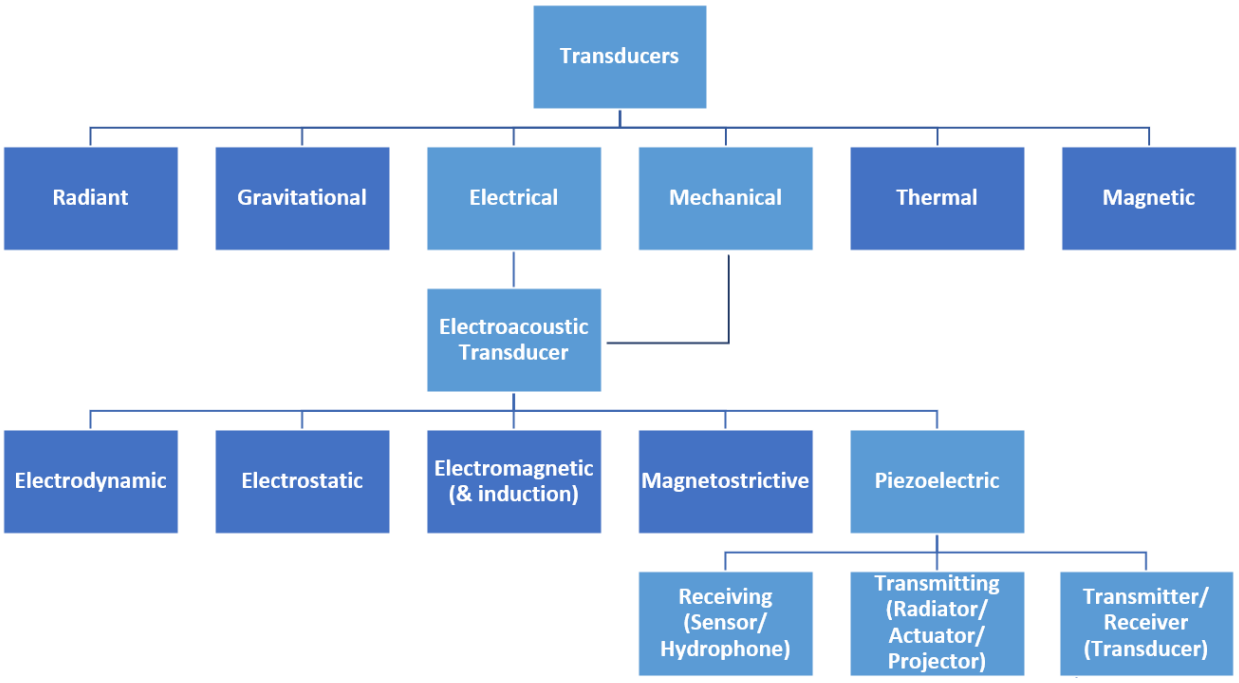

Figure 1. Classification of Transducers considered within this work [1], [7], [8].

This work focuses on the design and use of piezoelectric transducers as applied to underwater and in the medical spaces. Historically in underwater applications, piezoelectric transducers have been most used for their high piezoelectric properties and the ability to process them into different

forms. While the term “transducer” may refer to an entire sensing or projecting system, each piezoelectric transducer will contain a piezoelectric element at the core of its functioning. The surrounding components of a transducer help carry clear signals to contribute to its overall efficiency, but the “element” is responsible for the physical conversion of energy [8].

While specific subcomponents of a transducer vary per application, the piezoelectric transducers will consist of multiple subsystems expressed here in order of the energy flow from acoustic energy to electrical energy, as seen in Figure 2. From the transmitted medium, the acoustic energy propagates through the “casing/housing” of the transducer into a selected medium that acts as an “acoustic modifier” (such as a matching layer, coupling fluid, or backing layer) to have the acoustic signal behave according to the needs of the use case. The element turns the acoustic energy to electrical energy which is picked up by the “charge collector” (electrodes) and passed through a signal carrier (a wire and amplifying circuit) to be read out as an electrical signal. While the embodiment of these systems varies per transducer use case, these subsystems can be identified in most electroacoustic transducers.

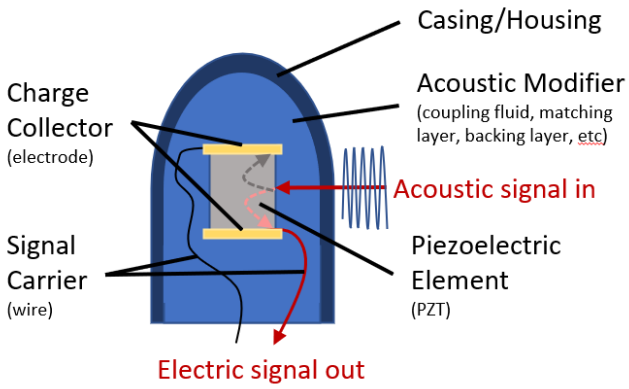

Figure 2. Transducer subsystem flow of energy. Acoustic energy is transmitted through the case and acoustic modifier before the piezoelectric element converts the acoustic energy to electrical energy. This is collected and output via electrodes and wires respectively.

1.1.1. Piezoelectric Materials

Piezoelectric materials are capable of converting acoustic energy (in the form of mechanical stress and strain) into electric energy (generation of an electric field and electric displacement)[9], [10]. This class of materials was first discovered by brothers P. Curie and J. Curie in the form of Quartz crystals [11]. The application of an electric field around such materials yielded deformations of the physical structure of the material [12]. Since then, multiple other materials have emerged as sharing these qualities, some requiring the action of "poling:" the action of applying a large electric field to the material for an extended period of time (about an hour) to activate the described piezoelectric effect [13]. This subclass of piezoelectric materials are known as "ferroelectric," and while they require the additional step of poling, their piezoelectric effect is greater [14]. Among these ferroelectric materials, Lead Zirconate Titanate (PZT) is one of the most easily processed materials with the highest performing piezoelectric effect[7].

Turning attention to the mechanism which enables the piezoelectric effect, Figure 3 shows the polarization which occurs when a piezoelectric molecule moves from un-loaded (a) to a loaded state (b). The combination of many molecules under compression (c) results in a dipole with fixed charges at each end [15]. When electrodes are applied to opposite sides of the material, charges at each end, and a voltage difference can be observed [16]. While Figure 3a displays an unpolarized molecule, it is worth noting that the poling process of a ferroelectric material may leave the material in a slightly polarized state. This is additionally associated with the non-centrosymmetric structure of PZT [9].

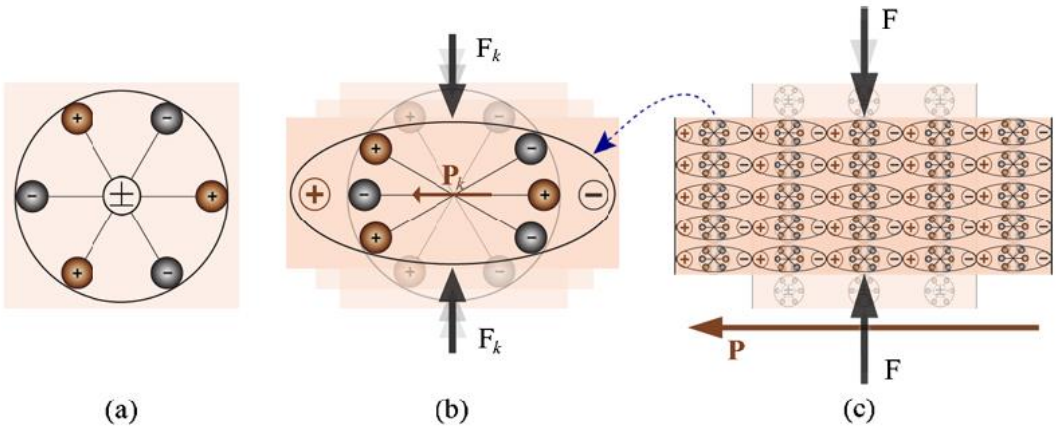

Figure 3. Piezoelectric Dipole: (a) un-loaded piezoelectric molecule. (b) compressed and polarized molecule. (c) Many molecules of a piezoelectric material under compression forming a dipole [15].

The extent to which a piezoelectric material outputs an electric response from an applied force is quantified by a ratio of charge to force and is generally notated in units of picocoulombs per Newton (pC/N). This material property is the piezoelectric coefficient, $d_{mn,}$ and it can be represented as a 3x6 matrix, regarding the direction of measured output voltage (m) and direction of applied pressure (n) relative to the poled "3" direction [17] [11]. The 3 components of this matrix we are concerned with, given our intended applications are d_{31}, d_{32}, and d_{33}. These are the coefficients resulting from compression on each side of a piezoelectric element when the voltage is collected along the poled direction [9]. These three components of the matrix can be summed to achieve the hydrostatic piezoelectric coefficient, d_h, wherein the element has pressure applied on all sides at once[18].

$$d_h = \Sigma d_{3n} \qquad \text{[eq 1.1]}$$

Using the hydrostatic piezoelectric coefficient, the piezoelectric voltage constant g_h ($Vm^{-1}Pa^{-1}$) can be determined][18], [19]. This term defines the strength of electric field produced by a piezoelectric material subject to a defined hydrostatic pressure.

$$g_h = \frac{d_h}{\varepsilon} = \frac{\Sigma d_{3n}}{\varepsilon} \qquad \text{[eq 1.2]}$$

Wherein $\boldsymbol{\varepsilon}$ is the absolute dielectric permittivity (Farad/m) of the piezoelectric element. The relative permittivity or dielectric constant, k, is expressed as a ratio between the piezoelectric material's absolute permittivity, ε, and vacuum permittivity, ε_0. ε_0 is a constant value of the permittivity of free space $8*10^{-12}$ F/m or C/Vm.

$$k = \frac{\varepsilon}{\varepsilon_0} \qquad \text{[eq 1.3]}$$

These piezoelectric properties come together in the context of hydrophone applications wherein the hydrostatic figure of merit (HFOM) is defined as $d_h * g_h$[19]. The HFOM is used to compare receiving transducers in many fields including underwater applications as well as medical [19]–[21].

1.1.2. Hydrophones

The transducer system presented in this work is designed to be an underwater receiving transducer. This is also known as a "hydrophone". Simply stated, a hydrophone is an underwater microphone. A Hydrophone is characterized by how efficiently it converts mechanical acoustic energy into electrical energy and at which frequencies the energy can be converted [6], [22]. This "sensitivity" (Mh) is read in as decibels (dB), referenced to 1V/μPa in accordance with the medium of water as opposed to air which is referenced to V/Pa. The sensitivity of a hydrophone in any shape can be calculated via equation 1.1 [7], [23].

$$M_h = 20 \quad \log(g_h t) \quad - 120 \qquad \text{[eq 1.4]}$$

Wherein g_h is the hydrostatic piezoelectric constant discussed in section 1.1.2. t is thickness of the element in the poled direction, and 120 is subtracted as a decibel conversion to transfer the sensitivity reference from 1V/Pa to 1V/μPa.

The sensitivity, as expressed in equation 1.1, assumes that the acoustic energy reaching the element is the full intensity of the incident acoustic energy at the position of the hydrophone. Since the face of an underwater sensing element will be separated from the water medium by protective casing, however, there will exist reflections, allowing only a portion of the acoustic signal to pass through to the core element [24]. Total transmittivity, T, is a function of acoustic impedances through which an acoustic wave passes as it propagates into the transducer element. The transmittivity imposes a fractional reduction of acoustic energy transmitted through a change in acoustic impedance. This fraction of transmitted energy is described by equation 1.2 [7].

$$T_{12} = \frac{2z_1}{z_1 + z_2} \qquad \text{[eq 1.5]}$$

Where z_1 and z_2 are the acoustic impedance of the mediums 1 and 2 respectively. Impedance, Z (rayl or Pa-s/m), is a property of a medium through which sound is propagates [25]. A visual representation of the acoustic behavior at a mismatched impedance interface is shown in Figure 4.

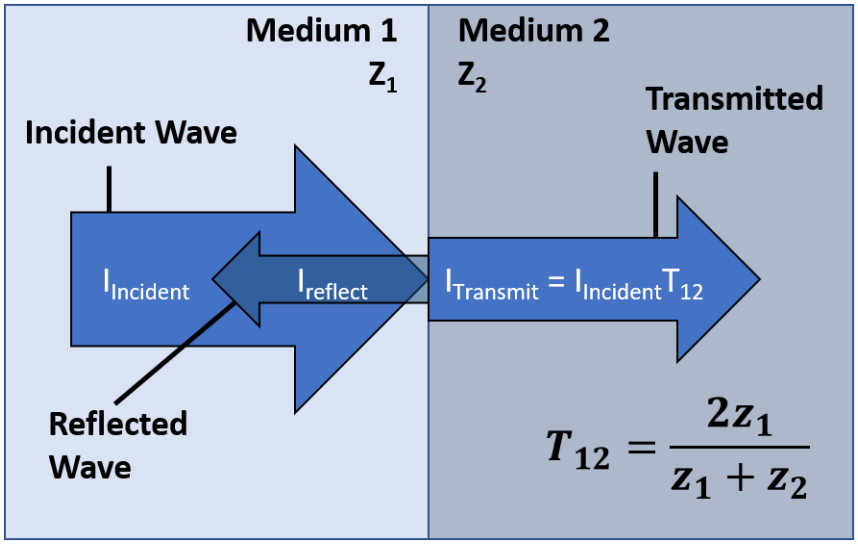

Figure 4. Incident sound transmission through a medium with mismatched impedance. A portion of the incident wave is reflected as it passes through the interface of impedance, Z_1 and Impedance, Z_2. The transmitted intensity, $I_{Transmitted}$ is only a fraction of the incident wave's intensity, $I_{Incident}$.[25]

A common source of loss for piezoelectric elements, regarding transmittivity, is the high mismatch in impedance between the piezoelectric element and its surrounding medium due to the high density of piezoelectric ceramics [23]. This is made clear through the equation for acoustic impedance:

$$Z = \rho c \qquad \text{[eq 1.6]}$$

Where ρ (kg/m^3) is density and c (m/s) is the speed of sound in the material, a property that increases with increased material stiffness or elastic modulus (MPa) and decreases with density [25].

$$c = \sqrt{\frac{E}{\rho}} \qquad \text{[eq 1.7]}$$

Piezoelectric ceramics, such as the one used in this work, PZT, has both a high density and a high stiffness modulus, making for a large impedance value and significant reflections during acoustic transmission. In this way, transitivity will come to affect the sensitivity of the hydrophone, as further expressed in chapter 2.

In addition to sensitivity, transducers are characterized by their resonance frequency. For a microphone or hydrophone, the point of resonance marks the highest frequency of reliable readings before sensitivity drops off [7]. This range of operational frequencies is known as the working range of the transducer. For an emissive transducer, the resonance is the point of largest displacement [7]. Applying an electrical signal at the resonant frequency will produce the greatest mechanical response or vice versa [8]. The working curves for a receiving/transmitting spherical hydrophone can be seen in Figure 5 to enable an improved understanding of the fundamental concepts.

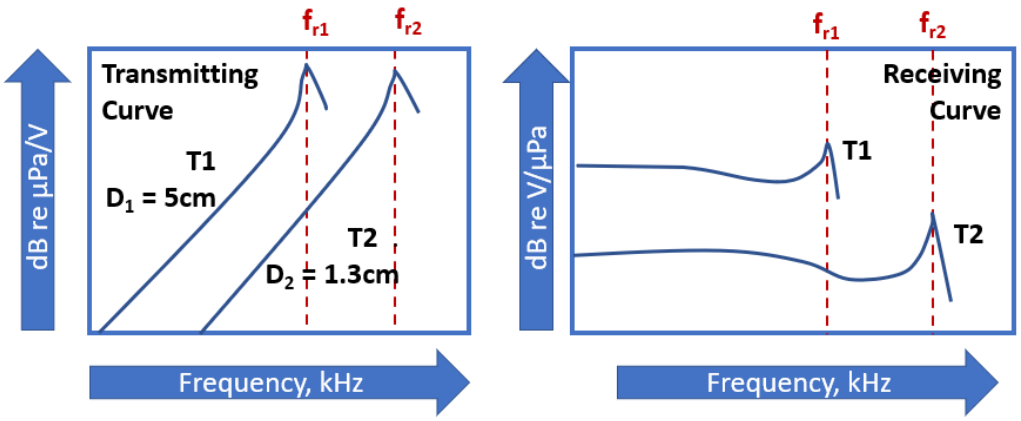

Figure 5. Response of the working range and resonant frequencies of two variably sized transducers from the F-42 spherical hydrophone family used at the USRD. Transducer 1, T1, has greater diameter than transducer 2, T2, yielding a lower frequency and greater response. General trends of transmitting and receiving responses can be observed [7].

Expanding on the value of knowing/selecting a frequency range and sensitivity of a hydrophone the beampattern is another aspect contributing to the value of a Hydrophone [26]. The beampattern of an acoustic transducer informs the difference in responsiveness of the transducer based on the direction of incoming sound. The Geometry of an acoustic element and the surrounding geometry of the transducer will influence the beampattern of the transducer[7]. A sphere, for example, ideally has a uniform beampattern, such that all directions will be equally responsive. For the standard hydrophone, whose piezoelectric elements are stacked cylindrical disks, the directivity is described by a constant responsiveness at all points circling the element on the XY plane that passes through the element. Variance from this plane in the Z dimension will produce varied response due to element asymmetry in this direction. The beam pattern is generally expressed in terms of sensitivity at a specific frequency, angle theta, and angle phi [25], [27]. For ease of geometric comparison between various beampatterns at a select frequency, normalization to the max value can be applied such that

$$M_{norm}(f,\theta) = \frac{M(f,\theta)}{M(f)_{max}} \qquad \text{[eq 1.8]}$$

Where M_{norm} is the normalized sensitivity at a selected frequency f, at a specific angle, θ, and $M(f)_{max}$is the maximum sensitivity at a selected frequency. It is assumed that this normalized beampattern considers only a 2D plane of directionality, holding φ, the angle coming out of the plane, constant[25], [27].

While most existing hydrophones are dipoles or omnidirectional, meaning they have lobes of higher responsiveness in the front and back or all around, there are used for other patterns [28]. If noise is loud from a particular direction that is not the intended direction of listening, having a beampattern to exclude this direction could prove to significantly improve the Signal-to-noise ratio (SNR). Ultimately, a hydrophone should achieve as large a signal as is intended with as small noise as possible, raising the SNR as high as possible[28].

1.1.3. Mask-Image Projection Stereolithography

Stereolithography or vat photopolymerization is the process of selectively shining UV light into a vat of photoreactive resin to instigate a photopolymerization wherein particles in the resin form polymer chains, linking together, and generating a solid. This is carried out to generate a single solid cross section of a part in the XY plane and is repeated layer-by-layer in the z dimension to produce a 3-dimensional part [29]. These crossections are developed by slicing a solid part into layers, down the Z-axis. The printing of resin in this way may be layered from the top down, where UV laser or image is shined down into a vat of resin or bottom up, where a UV projection is shined up through an optically transparent window into the bottom of a resin vat [29]–[31]. The direction of the motion stage on which the part is build is elevated gradually, up out of the resin, based on the method of curing as seen in figure 6.

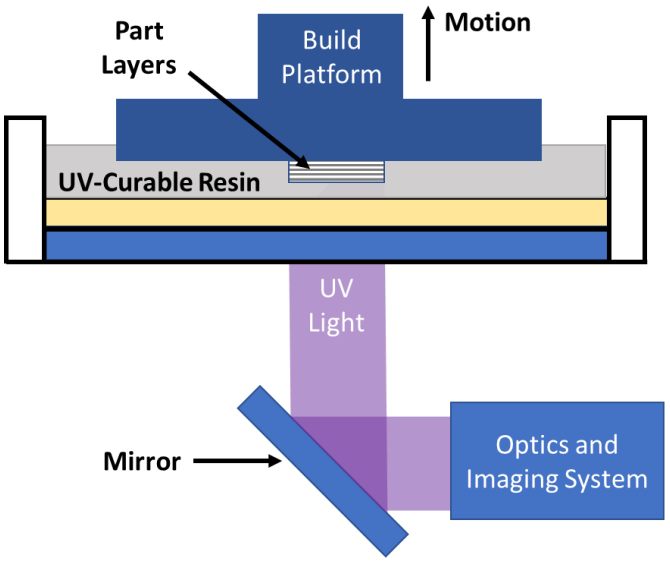

Figure 6. Bottom-up mask image projection Stereolithography (MIP-SL)

The Jacobs equation is a foundational in describing the behavior of curing a resin to generate parts via Stereolithography [32].

$$C_d = D_P \ln (E_{max}/ E_c) \qquad \text{(Jacobs PF (1992))}$$

The resin's cure depth is a function of the resin's properties: critical exposure, C_d, and depth of penetration, D_P. If the energy received by the resin at a point, E_{max}, does not exceed the critical Exposure, a characteristic of the resin, the resin will not cure, and no layer will be generated. The depth of penetration modifies the incident energy into the resin, so the addition of any light inhibitor (such as PZT particles) to the resin will reduce the depth of penetration. [32]

Whereas the Jacobs equation above is traditionally applied to a single laser traced through a 2-dimensional cross section, the use of a Digital Mirror Device, DMD, offers the ability to shine the entirety of a 2D cross section onto resin to instigate the curing of a full slice at one time. This process is called mask image projection stereolithography (MIP-SL), and it demonstrates a direct relationship between exposure time t of each layer and Cure depth [29].

$$C_d = D_P \, ed^{-E/Ec} = D_P \, e^{-H*t/Ec} \qquad \text{(4.30, AM textbook)}$$

The limited depth of penetration of a resin introduces a lower bound for the exposure time allowable to create a successful print; The layers must overlap sufficiently to ensure strong enough layer adhesion.

As we consider part strength, there are inherent limitations placed on the material properties being used. Since a photopolymer matrix is necessary to manufacture any part printed in this way, the brittle properties of photopolymers are inevitable [33]. When we consider high resolutions additive manufacturing such as the system created by the Zheng and his Additive Manufacturing Metamaterials Lab, the parts produced will be brittle and subject to damage even when simply being removed from the build stage [16], [30], [31]. This is one of many high precision printing methods [34]. To navigate this, sacrificial support struts can be used to separate the printed element from the build stage[16]. These support struts must withhold any forces the part is subject to during the printing process.

Thus, we seek to achieve the following relationship of force experienced by the print at any given layer, F_{print}, and force allowable by the support struts, F_{supp}.

$$F_{supp} > F_{print}$$

Since the process used in this work is bottom-up MIP-SL, the force experienced by the printed component is directly related to the viscosity of a resin being printed. Since the components being printed in this work consist of circular forms (struts and disks), the equation for Stefan Adhesion is used to predict the suction forces experienced by the print at each layer [35], [36].

$$F_{suction} = \frac{3\pi\mu u r^4}{2h^3} \sim F_{print} \qquad \text{(Stefan Adhesion equation)}$$

In this equation, a disk of radius, r, parallel to a surface is separated from a height, h, at velocity, u. The viscosity, μ, describes the medium or resin within which the disk is separated [36].

When forces of printing are too high, problems will arise in the form of defects and fracture. This imposes limitations to the freeform manufacturing method, and literature informs us that the intense suction force created by the high viscosity of particle-loaded resins such as that of PZT-loaded resin limits the printability [31], [37]. In recent years, additive manufacturing of particle-loaded materials via stereolithography has grown to be more widely adopted, and there have been multiple methods used to navigate the high forces felt by the printed parts subjected to a highly viscous resin [16], [37]–[43][43].

Most methods for reduce this significant force amid extreme viscosity involve use of a PDMS window. Since PDMS is an oxygen-permeable polymer, the use of the PDMS in this way creates an oxygen inhibition region, also called the “dead zone” [31]. The presence of oxygen in this dead zone prevents the resin from curing, such that a region ~2.5um from the surface of the PDMS window remains uncured [40]. Not only does this prevent the resin from curing to the production window, but it maximizes h, thus minimizing the force experienced by the printed part [37]. Recent work has additionally shown that there is a present reduction in this deadzone at higher exposure times [38]. While other methods of translating the print stage parallel to the PDMS window before lifting[37] and tape casting by spreading a thin layer of resin each layer [44] have been shown to improve printability, these methods require greater setup with additional degrees of freedom for moving along the x-axis or to enable an even spread during each layer. A traditional bottom-up vat in Figure 7 is used for photopolymerization with a single degree of freedom motion stage provides an efficient and accessible printing system, provided the forces can be appropriately overcome.

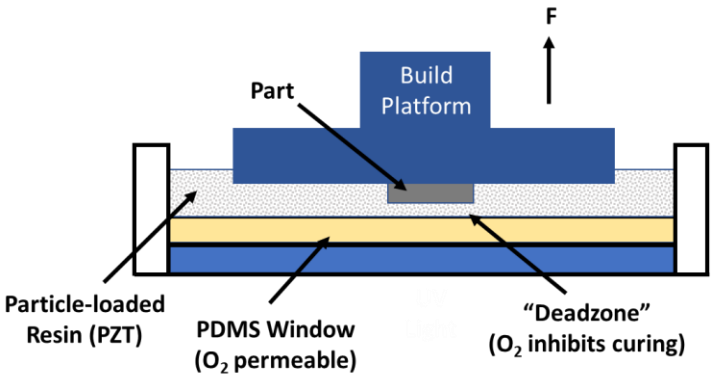

Figure 7. Particle-loaded stereolithography with PDMS window and oxygen-inhibited "deadzone."

With the foundation set up in this section, it can be gathered that the printing of a piezoelectric element will be possible in the form of various complex geometries. When this happens, the PZT nanoparticles will be mixed into a photopolymer resin and suspended in a cured photopolymer matrix upon curing [45]. At this point, the printed part is considered "green," as it still must be processed to achieve the intended state. The final step before poling is called "sintering" where the part is baked in a furnace to simultaneously remove the photopolymer from the PZT and allow the PZT to go through a process of "densification" to become a solid ferroelectric part [45]–[47].

1.1.4. Architecting Lattices

It is made clear that many intricate structures may be manufactured via means of additive manufacturing, and this even applies to piezoelectric materials. Geometries called lattices enable the modification of material behaviors by controlling porosity, structural load distribution, as well as material displacement [16]. While these geometries have previously too complex to manufacture or were not manufacturable on a small enough scale, the aforementioned advancements in additive manufacturing have enabled rapid printing of lattice geometries and the printing of latticed PZT [16], [31], [39]. The controlled tuning of the material properties in the

ways described is a process known as “architecting,” and it has become known to even modify the Poisson’s ratio of materials enabling negative values [48].

Whereas many porous materials studied over the past hundred years yield a similar modification of material behavior to those of lattices, these porous materials do not allow for a controlled and consistent porosity, whereas porous “foams” are stochastic[18], [20], [49].

Two distinct material properties tuned by latticing are density and the stiffness modulus [16]. The stiffness modulus or elastic modulus of a lattice is differentiated from the modulus of the source material through terminology of the “effective modulus.” This is the modulus of the material in its latticed state. A textbook for cellular solids outlines a model for effective modulus of a lattice as equation 1.9 [50].

$$E_{eff} = \alpha \bar{\rho}^{\beta} E_s \qquad \text{[eq 1.9]}$$

Where α is the pre-factor, $\bar{\rho}$ is the relative density, β is a modifier to account for differences in dominating modes of loading (tensile compression to bending rises respectively from 1 to greater than 2 respectively [16]), and E_s is the Youngs modulus of base PZT material after sintering.

The design of the lattice used in this work is based in a parameterized unit cell on the left of Figure 8, wherein the effective stiffness modulus E_{eff} can be controlled through the angle, θ and strut thickness d. The density ρ is additionally influenced by the strut thickness d, length l, and angle θ, indirectly through the relative density $\bar{\rho}$.

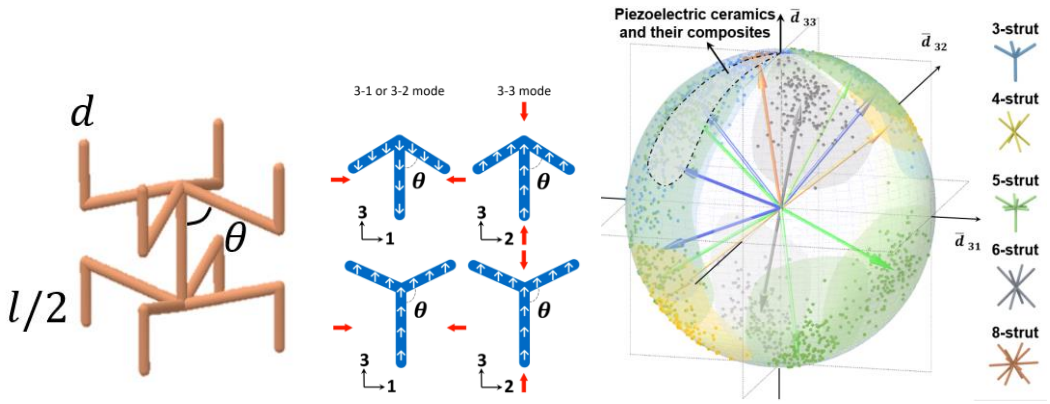

Figure 8. Tuned piezoelectric response**. (**left**)** Lattice unit cell, angle theta, strut length l, strut diameter d. (middle) lattice struts under compression: 75 and 120 degree. (right) modified response in d_{33}, d_{31} according to strut architecture [9], [16]

Since changes in screw angle theta modify the stiffness response, flipping the direction of polarization even, as seen between the 2 lattice cross sections in the middle of Figure 8 or in the image on the right, modifications to the d_h parameter under hydrostatic loading will compound to provide a range of tunable responses within a single material [16]. When the single unit cell with tuned material properties is repeated in the X, Y, and Z dimensions, the lattice is generated. This is imaged in section 3.2.1 when the specific unit cells and the number of unit cells are selected.

The density of the lattice is controlled and quantified through a measure called the relative density $\bar{\rho}$. The relative density is the density of the composite latticed material as if it were a single material divided by the density of the source material; this relative density is often considered in the context of a single unit cell [51]. The remaining "empty space" has a relative volume of $1 - \bar{\rho}$, and it is consumed by the medium in which the lattice resides [52]. This will be seen in many cases to simply be air, but some situations may use a fluid or other material to fill in the open space [20]. In figure 1.1.4, the "aspect ratio" is defined as d/l and this ratio drives the relative density of the lattice for a given angle theta.

The tuning of the elastic modulus and density will factor in to enable tunability in an acoustic context, as these will influence impedance as well as the piezoelectric parameters of the piezoelectric materials.

1.2. Current Ultrasound Applications in Academia and Industry

The ability to manufacture piezoelectric materials in unique geometries opens the doors to ultrasonic applications. This section provides a brief investigation into how latticing or porous materials have been used for such transducers in academia as well as assessing the uses of underwater ultrasound in industry. Insights are gathered from organizations, interviews, and literature.

1.2.1. Porous, composite, and latticed ultrasound

Porous and composite materials have been applied to the transducer creation even before 1980 with through the use of parallel ceramic rods embedded in a polymer matrix [21]. In 1985, advancements were made wherein acoustic materials could be designed to match the impedance of water by punching holes through PVDF film [23]. 6 years later, these concepts of ceramic piezoelectric rods and impedance matching were combined to enable an ultrasound element which matches the impedance of tissue for ultrasound imaging [53], [54]. From here, methods such as cold pressing of voided PZT and polymer impregnating were used to design porous hydrophone and receiving transducers[18], [20], [49]. While some of these works move towards variable response from variable loading methods, they are constrained in their geometries and demonstrates stochastic porosity [18], [20]. One commercialized transducer called the Sonopanel^{TM}, mimicking the parallel rod composite with a more effective process of ceramic injection moulding [55]. Porous materials were expanded to be applied in ultrasonic arrays before the presence of PZT additive manufacturing became prevalent [56]. With piezo composites being more commonly

printed, various geometries have been tested to yield improvements in emissions for medical and underwater use cases[42], [45], [57], [58].

The additive manufacturing of lattices has even turned to the space of tuning impedance for inactive materials such as a hydrogel to mimic the biology of a dolphin in achieving improved frequency ranges [59]. Tuning of lattices has also been used for inactive acoustic dampening in airplanes, and while this could be made actively dampen through correct manufacturing methods, this has not been done yet [60], [61].

The presented works have shown modification of material properties through latticing for improved performance of active materials or tunability of passive behaviors. None of these works offer a fine control of the electrical response to an ultrasonic stimulus, and none offer a tunability in all three directions of pressure for tuned g_h value.

1.2.2. Hydrophone/Underwater Applications

It is desirable to have different working ranges depending on the application, so controlling response of a transducer to be defined to a specific frequency range or to broaden the range would benefit users of transducers greatly. Considering developments of Underwater Sensor Networks (USN) and internet of underwater things (IoUT), there are needs for improved short range communication and signal-to noise ratio underwater [62] [63]. Population monitoring, oceanographic data collection and bioacoustics studies have outcomes that are directly linked to the quality of data collected [64], [65]. Calibration hydrophones and measure acoustic noise are the generalized applications expressed by published navy reports, but there is a need for a low signal to noise ratio[66] Hackathorn, Hugus, and Groves have describe their hydrophone developments, including the need for sensitivity, resonance and beam pattern control [22], [26],

[66]. To back this up, work on a small autonomous towed array expresses the many sources of noise and their associated directions in naval sonar [67].

1.2.3. Medical Application

While it is clear there are ample applications for the underwater space, with more unlisted, there is still another world of applications in the medical space. A few key areas that can benefit from uniquely tuned geometries at high resolution and high piezoelectric response are described. High intensity focused ultrasound (HIFU) has been shown to emerge as a prevalent use for additively manufactured impedance matching layers [13], [68]–[70] and custom element geometries [42], [45]. Some spaces this may be applied is for transcranial doppler (TCD) techniques to measure cerebral blood flow velocity [71], ablation of dangerous cells in the body [13], etc. Conformal arrays for the body can additionally be generated for wearable sensors for health monitoring[72], [73]. Lastly, contactless ultrasound power transfer (UPT) systems may enable contactless charging of devices for implanted devices in the body [74]. While the possibilities continue, it is clear there are ample opportunities that will come from the medical space regarding the high-resolution freeform printing of piezoelectric.

1.3. Motivation

The world becomes increasingly driven by data, as it is used to monitor and predict and model the world around us [2]. When this data interacts with the physical world, it is embodied through actions such as the movement of a robot arm to a precise location, the reading of a pulse during health monitoring, underwater communication over a distance, and much more [75]–[77]. During these data-heavy processes, there must be a reading in of data (via sensors) and/or an interaction with the world based on the data. Electroacoustic transducers can receive or emitting sound to

enable acoustic monitoring, spatial imaging, imposition of acoustic pressure, and even the transfer of energy through solid matter [73], [74], [78]. All these methods have significant applications at ultrasonic frequencies.

With the prevalence of additive manufacturing growing to enable mass customization, recent published work in additively manufactured transducers [10] provide a framework for precise tunability. The freedom of form brought about in these same spaces enables the creation of transducers small enough and complex enough to produce designed ultrasonic acoustic fields and high-intensity acoustic pressures [74], [78].

Given the stated strides in additive manufacturing at scale, geometry, in tandem with developed an awareness of effectively tunable properties through latticing, there are great opportunities to enhance the field of ultrasound with lattices and other atypical geometric elements. These improvements will enable more effective interfaces with the world through sensing and actuating.

Improvement of printability through modelling in this space will additionally help to propel these technological advancements even further in the possibilities of manufacturing sensor elements.

Considering hydrophones alone, section 1.2 has expressed that there are many applications that can greatly benefit from improved SNR. Unlike earlier works, a single-element hydrophone can achieve any shape of desired directivity pattern. This enables a better Signal-to-Noise Ratio at a mechanical level, enabling better, cleaner data. This has potential to reduce the circuit complexity and enable a low computational cost for directional recognition. Some solutions which can be generated from this technology may even allow for minimal processing power in achieving system awareness relative to a surrounding environment. This is further discussed in Chapter 8.

1.4. Structure and Contributions

This paper contributes in multiple ways across many spaces, and the main contributions are narrowed down to 4 quantitative contributions and 3 contributions of theory and approach. Chapters 2, 4, 5, and 6 are quantitative in their contributions whereas chapters 3, 7 and 8 are contributions of methodologies or frameworks. These chapters are seen structured in Figure 9.

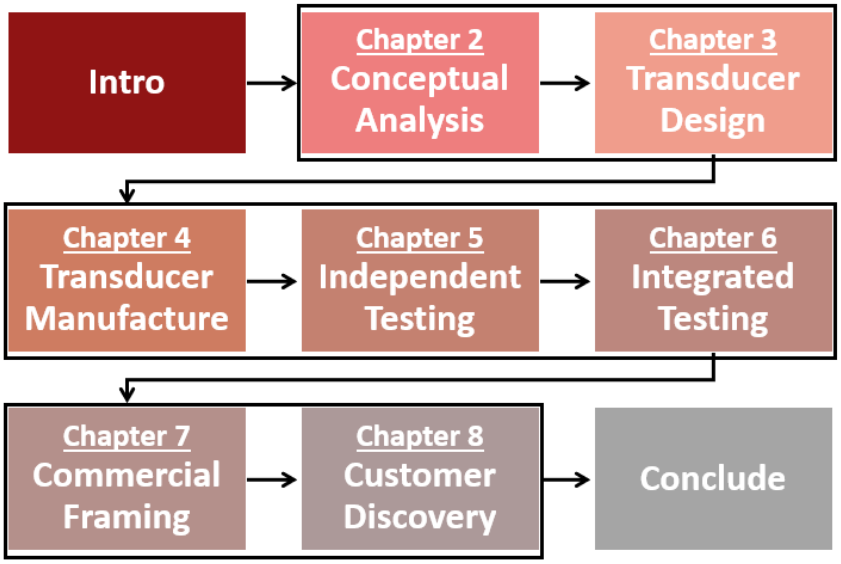

Figure 9. Flow chart illustrating a high-level overview of the present work.

Chapter 2 contributes a theoretical operating range from a proposed model for theoretically calculating a latticed hydrophone's sensitivity, resonance, and beam pattern. Chapter 3 proposes a framework for rapid testable transducers of adaptable form. Chapter 4 provides a model to improve printability of parts based on support strut design and predicted force loading amid PDMS wear; the chapter finishes with the manufacturing of the elements to be tested. Chapters 5 and 6 contribute designed testing and analysis of latticed ultrasound elements for tunability of response in sensitivity and resonance followed by beampattern of integrated-element lattices. Chapter 7 proposes a method for rapid personalization of a continuously tuned lattice elements. Chapter 8 demonstrates a method for identifying problem spaces to match to a developed technology.

Overall, the work carries out and reveals a workflow from conceptualization through modelling into first steps to commercialization via the "technology push." Such a path is common for academics, and while many projects are funded, thus communicating an initial demand for the technology, the technologies that emerge may go unused in other highly applicable spaces. Observing the path from a concept to a commercially framed technology will enable great expansion of technology into the broader world for the potential of bettering society.

Chapter 2: Conceptual Hypothesis

At the core of a novel technology is the combining of two or more ideas into a new "novel" idea. In this case, the concept of architected lattices is combined with transducers at the base piezoelectric element. Thus, it is hypothesized that the architecting of lattices across an element will selectively tune the element, controlling for sensitivity and resonant frequency. Through directional tuning of these characteristics, the beampattern can be designed both in-plane and omnidirectionally.

2.1. Predicting Sensitivity

In predicting the sensitivity of a latticed element, we start by referring to the sensitivity equation: equation 1.4. The Voltage constant, g_h is described in section 1.1.2, and when considered in the context of equation 1.4 there is an opportunity to use lattice architecting to tune this g_h constant from both d_h as described in section 1.1.5, as well as the permittivity of the hydrophone elements.

Using lattices, the absolute permittivity can be modified as well. The following expression is derived from Lifson et al's the equation for absolute permittivity of a composite lattice [79].

$$\varepsilon = \left[\bar{\rho}\left(k_p - k_m\right) + k_m\right]\varepsilon_0 \qquad \text{[eq 2.1]}$$

Here, $\bar{\rho}$ is relative density of the lattice, k_p and k_m are the dielectric constants of the base piezoelectric material and the medium surrounding the lattice (~1 for air), and ε_0 is vacuum permittivity. By tuning the relative density, $\bar{\rho}$, of the lattice, lower permittivity, ε, values can be achieved. The piezoelectric charge constant, d_h, through use of micro-architected lattices expressed by Cui, can be combined with this permittivity at select relative densities to produce a higher piezoelectric constant, g_h. This heightened g_h influences greater sensitivity from a hydrophone using the element [16].

We recognize the need for parameters g_h and thickness t of the element, but we must also consider the impedance mismatch occurring, as the predicted reduction in acoustic impedance will enable increased transmittivity through to the lattice element. That is less reflections across the multiple impedance-mismatch interfaces. Referring to equation 1.5 for transmittivity and recognizing the acoustic wave propagation as a series interaction, the presence of multiple impedance mismatches requires the transmittivities of each mismatch to be multiplied to achieve a total transmittivity across all media, T as in equation 2.2.

$$T = \prod_1^n T_{n,n+1} \qquad \text{[eq 2.2]}$$

where 1 represents the first medium and n represents the final medium through which the acoustic signals will propagate. Factoring T from equation 2.2 into equation 1.4, we get a general expression for transducer sensitivity [dB re 1V/uPa].

$$M_h = 20 \quad \log(g_h t\, T) \quad - 120 \qquad \text{[eq 2.3]}$$

Since the d_h and permittivity, as used in equation 1.2 to calculate g_h, can be tuned through the architecting of lattices, the fundamental element responsiveness can be controlled, and even compounded based on the manipulation of the positivity or negativity of d_{3n} constants as expressed in section 1.1.4.

In addition to the benefits of tuning g_h, the modification of relative density additionally enables greater transmittivity, T. When consider the energy loss referenced in the section 1.1.2 from impedance mismatch and combine this with speed of sound through a material, we see a positive correlation of ρ as the tuned density with respect to relative density and stiffness modulus, as is controlled by the screw angle. This is easily observable in the combining of equations 1.6 and 1.7 to observe the positive relationships to impedance Z in eq 2.4.

$$Z = \sqrt{\rho E} \qquad \text{[eq 2.4]}$$

Lattices enable control over the density experienced by the composite material via relative density. This can be factored into the behavior of the piezoelectric lattice's acoustic impedance using the rule of mixture [23], [53], [54]. While we recognize the changes in elastic modulus may be experienced by the use of various lattice structures, we assume the base material properties of stiffness dominate in this model and that the mixture of elastic modulus will mix in accordance to the rule of mixture.

$$Z_c = \bar{\rho} Z_p + (1 - \bar{\rho}) Z_m \qquad \text{[eq 2.5]}$$

In this model, Z_c, Z_p, and Z_m are the acoustic impedance of the composite lattice, piezoelectric material, and the medium surrounding the lattice, respectively. $\bar{\rho}$ is the relative density of the piezoelectric material, as described in section 1.1.4.

Since the acoustic impedance of piezoelectric material is relatively large (>30MPa-s/m), reducing the relative density of the piezoelectric lattice will affect equation 1.5, achieving higher levels of transmittivity than those achievable by bulk piezoelectric materials. When considered in the context of equation 2.3, this enables potentially higher magnitudes of response and further controllability of transducer sensitivity.

2.2. Theoretical Sensitivity Range

Using equation 2.3, we can predict the sensitivity range achievable by this method. We calculate g_h, based on d_{31} and d_{32} values from Cui et al. [16], combined with permittivity values calculated through equation 2.1 to have an achievable range of g_h ~[-6.3E07]—[2.97E09]V/m [80]. A thickness 6mm was selected based on the product design in the latter half of this chapter, factoring in a >50% reduction in size during sintering. The transmittivity of the element, regarded as a composite, ranged from T ~.329—0.044. The range comes from the acoustic impedance mismatch between a piezo composite of relative densities 0.05 to 1. The relative density of the

element is modified to tune the acoustic impedance of the composite with equation 2.5. The resulting Sensitivity range achievable through these ranges is between 5.72dB and -23.3dB re 1V/μPa.

2.3. Predicting Resonance

A piezoelectric element's working range is defined by its resonance frequency, which is a function of density, young's modulus, and geometric form. Hugus expresses a lumped model for natural frequency of a hydrophone which considers a base-excited mass with a parallel linear spring and viscous damper [66]

$$f_r = \frac{1}{2\pi}\sqrt{\frac{k}{m}} \qquad \text{[eq 2.6]}$$

where k is the mechanical spring constant and m is the mass. The 2π term converts the frequency into Hz. The use of lattices enables manipulation of the element's compliance factor by modifying the lattices Effective modulus. By integrating the properties of Hooke's law into the spring-mass model, we reach equation 2.6. Hooke's law tells us that the spring constant, k, is equivalent to the force per length of extension for the element [81]. We use this Hooke's law, assuming a constant proportionality constant k to derive equation 2.7.

$$f_r = \frac{1}{2\pi}\sqrt{\frac{E_{eff}A}{tm}} \qquad \text{[eq 2.7]}$$

where E_{eff} is the effective modulus of the lattice composite, which is combined with its cross-sectional area, A, to yield the force component of Hooke's law. t is thickness, and max deformation in Hooke's law, of the sample (distance between electrodes). m is mass of the sample.

By combining equation 2.7 with equation 1.9, the equation for the effective stiffness modulus in latticed materials, equation 2.8 is synthesized.

$$f_r = \frac{1}{2\pi}\sqrt{\frac{\alpha\bar{\rho}^{\beta-1}E_s}{t^2\rho_s}} \qquad \text{[eq 2.8]}$$

where ρ_s is the source density of the sintered PZT material.

2.4. Theoretical Resonance Range

Resonance of latticed transducer elements is calculated though equation 2.8. [16] defines achievable alpha and beta values at ~0.2-5 and ~1.2-2.2 respectively. These values are enabled by the printable range of relative densities from ~0.05-0.45. Using Cui's measurements of bulk PZT, E_s = 480MPa, and bilk PZT density, 1360kg/m^3, the resonance could be calculated at various element thicknesses. At 0.06mm, the lattices range in resonance from 1.5kHz-41kHz. By the shrinking the thickness to only a couple unit cells, 200kHz and greater are achievable.

2.5. Beam Pattern Prediction

Since each different lattice screw angle is hypothesized to behave differently in working range and sensitivity, lattice designs can be combined to produce an element with controlled response in select regions. This is effectively designing the beampattern to fit the needs of a user. The frequency range will be modified as well to achieve different frequencies per element, but this aspect will not be considered in this work. To predict various lattice combinations, the expected sensitivity responses of various select lattice types are normalized with equation 1.8 and plotted on a polar plot where θ is degree of rotation or direction of incident sound, and $M(f,\theta)$ is the normalized performance out of 1 at a constant out of plane angle, φ. For the prediction, two predicted lattice sensitivities with from opposite sides of the predicted range are selected and plotted in Figure 10: high density 90-degree screw angle and low density 75-degree screw angle.

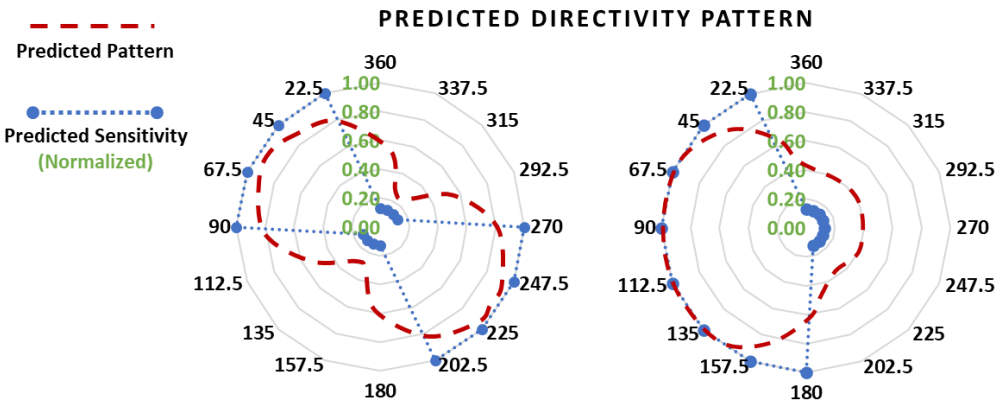

Figure 10. Predicted sensitivity pattern of predicted sensitivities plotted on a polar graph and blended at stiffness interfaces to consider the interaction in the predicted pattern. This is shown for 2 patterns: (left) alternating sensitivity across the diagonal and (right) half high sensitivity/half low sensitivity.

As seen in Figure 10, smooth line is to be generated to pass through established points on the polar coordinate system with a prediction that the interface between two lattice types (two screw angles or relative densities) will interact in behavior, pulling toward the mean of the two lattices. The expected plots shown here are generated with specific intended combinations of lattices to be manufactured in Chapter 6. This allows for a comparison with the experimental results from beampattern or directivity pattern testing.

Chapter 3: Framework for Transducer Design

While the elements of the transducers are at the core of the concept which drives the novel design, underwater transducers are subject to the conditions of water, and the pace of research demands rapid testing capabilities.

In order to efficiently test all lattice behaviors as well as the generation of other freeform transducer designs, a transducer framework was developed. This chapter outlines the overall structure of the framework, the specific materials selected for the consistent generation of hydrophones, out of architected lattice elements, and the decision rationale behind the selections.

3.1. Transducer Framework Overview

The transducer system is designed to be an underwater receiver of acoustic energy. This is also known as a “hydrophone”. Based on the underwater context and the need for a rapidly producible method for testing elements of variable size or form, the transducer is decomposed into the following subcomponents as shown in Figure 11, listed from the inner-most subsystem, and moving out. The subcomponents align with the generalized subsystems identified in Figure 11, and are accompanied by their respective function within the system.

- PZT Element……. Convert acoustic signal to electric (piezoelectric element)
- Coupling Fluid……... Carry acoustic signal through element (Acoustic Modifier)
- Painted Electrodes……. Secure element to casing, carry signal (Charge Collector)
- Casing (form, material) … protect element from water, (Casing/Housing)
  reduce acoustic reflection to element
- Shielding…… mitigate EM Interference (Signal Carrier)
- Wiring/Cable ……... protect/carry signal to be read out (Signal Carrier)

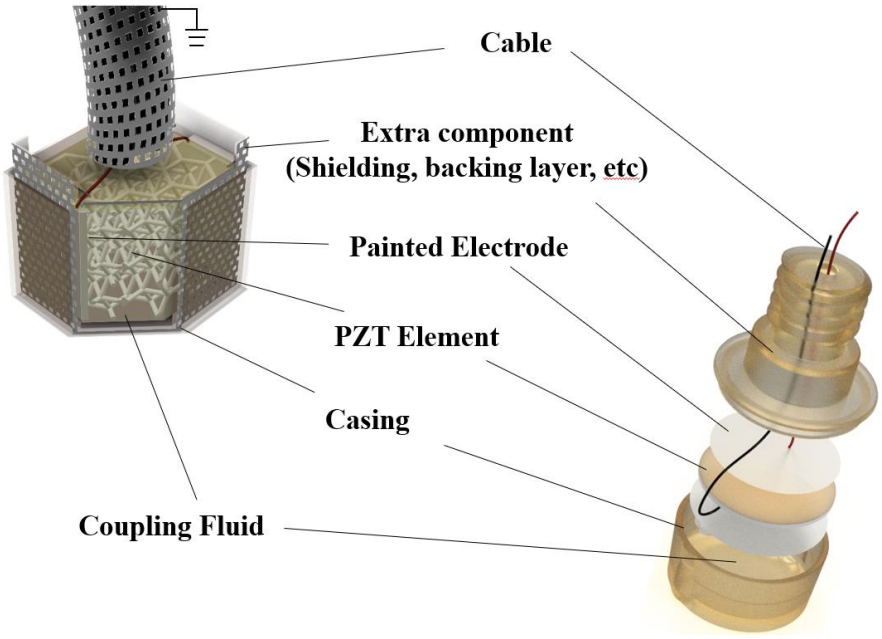

Figure 11. (left) Hydrophone System and Labelled Subcomponents and (right) High intensity focused transducer with larger piezo element, making it harder to print

3.2. Subcomponent Design and Selection Rationale

The design and selection rationale are all traced back to the context of the research, striving for a rapid timeframe with the high adaptability of form and the best performance possible, given consistency in all factors other than the elements being tested can be achieved.

3.2.1. PZT Element

To achieve the highly complex lattice structures and other considered freeform transducer designs, the piezoelectric element was 3D printed. A lead zirconate titanate (PZT)-loaded resin, capable of high responsiveness, was selected as the material based on technologies and experience within the lab. PZT is additionally shown to mix well in resin, have a relative low cost, and high piezoelectric abilities [9]. It is believed that the formula generated by lab mates would enable greater responsiveness than other 3D printed piezoelectric materials used in past literature [16]. To achieve the high resolution necessary while printing with a particle loaded resin, a custom Mask-

image-Projection Stereolithography (MIP-SL) system is used with a PDMS window as shown in figure 1.1.3.

The selected geometry for the hydrophone uses the lattice structure from the unit cell in figure 1.1.4. This structure is modified to block on relative density of the lattice and strut angle. two sets of lattices were designed: high density and low density. Each set includes three strut angles, named according to literature and with recommendations from Cui: 75 degrees (Auxetic, A, or re-entrant), 90 degrees (Foam, F), and 120 degrees (Honeycomb, H) [9] [16]. While these strut angles shown in a 2D profile in Figure 12 and their varied densities do not entirely encompass the operable range of these transducers, they provide a comprehensive range through which tunability can be observed while maintaining printability within a reliable range.

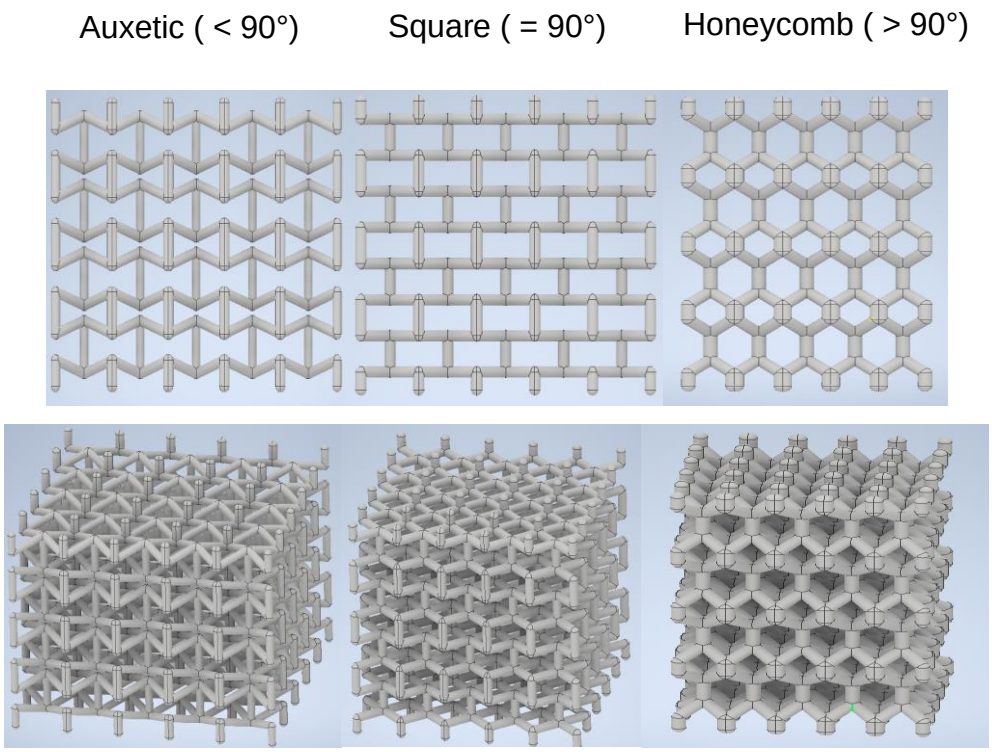

Figure 12. (top) Two-dimensional projections of the selected three-dimensional lattices. (Bottom) images of latticed CAD models

The three strut angles will influence the sensitivity through gh and the effects on resonance angle, and the strut thickness/length will influence the impedance, thus the system's transmittivity.

The lattices are maintained at least three unit-cells long on all dimensions to enable bending-dominated lattice performance[16]. The lattices are printed as cubes for simplicity of experimentation and maximized uniformity of elements as the element is further processed (sinter, poling, assembly).

3.2.2. Electrodes and Wiring

To read out an electrical signal resulting from deformation in a piezoelectric element, the charge difference between the sides of an element must be collected through an electrode and transmitted through wires to the cable where it is carried to the readout instrument.

Four materials were considered for the electrodes: copper tape, conductive copper paint, conductive Silver paint, conductive silver epoxy.

All materials were readily available within the lab, enabling same-day manufacturing and assembly. If these did not align with the performance needs, delays would ensue. The copper tape, while usable for poling, would not be able to contour to the freeform transducers as would be necessary for the design framework.

When comparing silver and copper paint, the lower electrical impedance of the silver was preferred. While both the conductive silver paint and the conductive epoxy enabled selective placement of the electrode, the high viscosity of the epoxy made it difficult to work with in tight spaces. This is discussed in chapter 4 during lattice manufacturing.

The silver epoxy demonstrated capacity for selective placement in hard-to-reach locations and had an added benefit of allowing for error in a surface when applied with a thickness of approximately 400μm. Since the piezoelectric element is 3D printed in a resin matrix, sintering

must take place to remove the resin and enable a high dielectric constant. The current sintering yield deformations in the elements which can cause lack of contact to the electrodes.

0.01mm wire was used to connect the electrodes to the transmitting cable.

3.2.3. Coupling Fluid

Coupling fluid lies in the void space between the struts of the piezoelectric lattice and any void space that becomes present within the bounding volume of the transducer casing.

An important assumption in this work is that acoustic waves will propagate through the latticed element as if it is a bulk material. In this way, equation 2.5 embodies the assumption of tuning acoustic impedance as done by Moffet and Powers [23]. Since this void space in this equation contacts, the PZT and the electrodes while having a significant impact of the behavior of the acoustics, design constraints are present for the selection of a coupling fluid.

The coupling fluid must: not dissolve silver or degrade PZT (chemically compatible), not be conductive, maintain an acoustic impedance between that of the casing (or water) and the latticed PZT element, be viscous enough to flow between the struts of the lattice element, be readily accessible to the lab

The following mediums were considered: Canola oil, Vegetable oils, and 200 cSt viscosity silicone oil [80], [82].

The considered mediums, acoustic impedances were determined through readings and calculations. When compared to the acoustic impedance of room temperature water, 1.48 MPa-s/m (the medium through which the lab is testing), Castor oil yielded closest impedance match of 1.463 MPa-s/m. The decision to use Castor oil was additionally supported by an analysis by Hackathorn's analysis of hydrophone coupling fluids [22]. The quick and low-cost accessibility of the Castor oil made it an ideal fit.

3.2.4. Casing (Form)

The case is designed to contour the form of the element volume, enabling the intended functionality of a freeform design while protecting the internal components of the transducer from material degradation or damage and potentially improving propagation of energy through an impedance interface[25].

The transducer casing is designed by first establishing the bounding volume of the piezoelectric element. In the hydrophone design, this was completed by measuring the length, width, and height of the PZT element, noting which surfaces were to be used as electrode surfaces. A CAD model of the bounding volume is generated, and a surface is offset from the volume, based on the tolerances necessary for the resolution of the 3d printer being used. The resolution combines with deformations resulting from a very small wall thickness (300um) and overcuring demanded a tolerance offset of 0.1mm from the bounding element volume. This offset establishes a surface from which the case wall is generated.

A parameter of wall thickness is assigned to the design for case walls. The wall thickness was limited by the AnyCubic Photon printer capabilities, the resin's printability, and brittleness of the material used at low wall thickness. The wall thickness is parameterized for ease of modification.

While ultrasound literature discusses the design of an acoustic matching layer of one quarter wavelength thickness to improve acoustic energy propagation through impedance mismatch (such is seen between the PZT element and its surroundings) , this technique provides a narrow frequency bandwidth [59]. Since the case design workflow proposed in this work is intended for use across a broad frequency range, modification of the wall thickness will be necessary based on the intended transducer operating frequency.

In order to control for performance variability from wall thickness, based on the needs of our experiment, wall thickness is maintained at the lowest achievable wall thickness, 210um.

Once the walls have established a “shell” around the piezoelectric element volume, the volume is segmented according to the volume geometry. This segmentation allows for element insertion after the case is printed, and must consider the function of holding fluid, routing wires, and allowing space for coating of adhesives/electrodes based on the particular use case. In the case of the hydrophone, the segmentation was placed at the top of the bounding box such that a lid was formed.

Lastly, a port or ports are cut into the case, generally within close proximity of the electrode locations such that wiring can be routed out of the case and attached to the cable.

3.2.5. Casing (Material)

The case material will be a significant factor in the performance of the transducer. Any mismatch in acoustic impedances between the case and its neighbouring mediums (i.e. Water or coupling fluid) will result in reduced energy transmitted to the sensing element. This is a result of reflections redirecting a percentage of acoustic energy [7]. In addition to impedance needs, the material will need to be compatible with the electrode, will need to withstand pressures of the use case, and will have to be accessible.

The applications within this work demand acoustic waves to travel through water, castor oil, and human tissue. All these mediums are a similar in magnitude, so the impedance of the case material shall be similar to mitigate reflections as much as possible.

It is recognized that a precise match will be very difficult to achieve and is outside of the research scope, so variance from the 1.48MPa-s/m may be necessary. Since the piezoelectric element is assumed to be a single composite material within the hydrophone, and some complex solid geometries will not need coupling fluid (depending on the application), it is realized that transmission from the case to a higher impedance medium (PZT or PZT composite). According to

Equation 2.5, this would drive a preference to have a material impedance for the case greater than the 1.48Mpa-s/m of water in order to assist with the impedance mismatch.

Lastly, the material must be accessible to the lab in large quantities for rapid prototyping and must be printable on the AnyCubic Photon.

Polyethylene (glycol) diacrylate (PEGDA) is a material quickly mixed within the lab at low cost and in large quantities. With an impedance just above that of water at 1/7Mpa-s/m and a knowledge that the material works well within the printing limitations of the lab, PEGDA was selected as the material for case manufacture [33].

3.2.6. Shielding

Upon testing pre-shielding, the hydrophone design read out voltages readings that precisely mirrored that of the signal emitted. It was too perfect… Electromagnetic Interference (EMI) was the cause. The solution of a wire mesh was considered, but bulkiness and too high impedance of the wire mesh led to the adoption of a conductive mesh tape. The tape was to be cut into a folding pattern to contour the hydrophone form. Grounding this shielding through the receiver cable, the EMI could be mitigated.

For additional protection of the shielding, an additional PEGDA layer is printed to compress the shielding against the original case.

Whereas this subcomponent is not necessary in many applications, there may be other modifications that will be necessary to successfully generate a transducer for an alternate use case. The ultrasound transducer for medical applications, for example, uses a backing layer that required an allowance of space layered behind the piezoelectric element's bounding volume during the case design workflow such that a backing material can be injected to prevent echoes from behind the element [78].

3.2.7. Cable

The transducer cable transmits the signal from the transducer's electrodes to the read-out device. Cable selection for hydrophones is very important, as uses will demand more than 100 feet of cable. At this scale, attenuation from capacitance in the wire is significant, and noise will be evermore present. Since the wire will be submerged in water for long periods of time, and subject to high pressures, the water permeability of the cable is a critical concern. Comparison of five cables, three from Beldin, one from DX, and one cable from Custom Teledyne Marine. While some cables required further quote requests for further insight, it was believed that the Beldin Coax 9862 retained the lowest capacitance per ft at 13.5pF/ft and used a PVC wire jacket, resisting water leakage. Unfortunately, all cables were out of stock or required a large lead time and costs outside of the project budget.

To enable the rapid pace of design, manufacture, and testing, a faster and lower cost solution was carried out. Bundles 3 ft shielded coaxial male-to-male cables were ordered from amazon. While the cables have poor water resistance, preventing long term use underwater, the lab experiment conditions enabled the hydrophones to be submerged for only brief periods of time during testing. The high volume available at a low cost and short lead time made up for any leakage problems, as a new cable could be quickly used if an old one demonstrated faulty behavior. This allows for the quick generation of many hydrophone samples, for rapid testing of all 6 piezoelectric element types. The short cables length additionally limited signal attenuation. The cable make-up is shown in Figure 13, and the EMI-mitigating tape was connected to the copper braided ground.

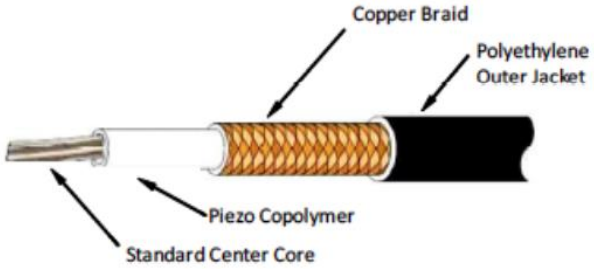

Figure 13. Diagram of rapidly available cable

By cutting the cable and stripping back the rubber to expose the coax center, the electrodes could be soldered: one to the positive wire and one to the shield-connected ground.

Chapter 4: Transducer Printing and Assembly

With a design in mind the next step is to build and assemble the transducers. This chapter starts with a novel model and method for support parameter generation to enable prediction of printing success. This model is used to inform the successful additive manufacturing of the acoustic elements. The element creation is followed by post processing steps to enable a high piezoelectric effect and the assembly of the elements. This is demonstrated on both a HIFU emissive transducer in addition to the latticed hydrophone elements described in chapters 2 and 3.

4.1. Printing Elements

Fabrication of the piezoelectric element takes place via bottom-up Mask-Image-Projection-based Stereolithography (MIP-SL) on a lab-built system [16], [83], [84]. As pointed out in the background, the system enables high resolution layer-by-layer curing of particle-loaded resins. This enables detailed lattices with a minimum strut thickness less than 300μm. While the vat photopolymerization process used here enables freeform design and high-resolution features, the use of the PZT-particle-loaded resins at small scales accentuate problems faced during high resolution bottom-up stereolithography such as slow print speed, surface finish, etc [40]. This limits production of lattices designs and other transducer forms. The reduced depth of penetration, material brittleness, and high viscosity are all considered as influential factors during the printing of the elements.

4.1.1. Forces Experienced by the Printed Part

Section 1.1.3 describes the initially predicted forces applied to a printed part of circular geometry. The parts printed for the manufacturing from the viscous PZT elements were lattices for hydrophone applications and a curved emissive element for medical applications, both crossectional geometries represent circular crossections, and while the lattices vary from this as

their horizontal struts are printed, the thinness of the struts makes forces relatively small. For this reason, the forces modelled in the Stefan Adhesion equation from section 1.1.3 act as a basis for the forces experienced by the printed part. Recapping, the supporting members of the print must exceed these forces to successfully complete a print. A diagram of such support forces is shown on the right of Figure 14 along with a free body diagram of the forces on the left.

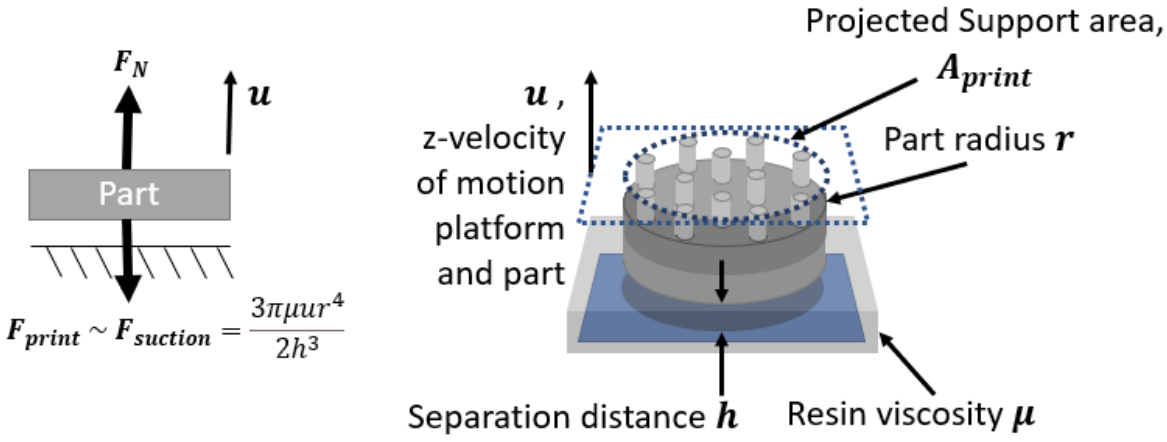

Figure 14. (left) free body diagram of considered print forces, calculated via the Stefan Adhesion Equation equal to $F_{suction}$. (right) the printed structure on the right is attached to the print stage at the dotted region. Struts are uniformly distributed across the surface of the element, and Stefan adhesion parameters are labelled.

Adding to the difficulties and limitation of SLA printing discussed in section 1.1.3, there are other present factors more difficult to quantify. In recent literature, Kunwar (2020) demonstrates the reduction of the oxygen-rich inhibition layer at increasing exposure levels, and Song (2016) expresses the deformations experienced by the negative and positive stage motion through compressive and suction force[38], [40]. This incurs cyclical wear on the PDMS film, compounded by a reduced h value experienced through exposure times. Since no models for this are present in current literature involving modifications to h from these factors, they were not to be considered unless necessity demanded.

4.1.2. Support Structure Design

In order to successfully print piezoelectric elements, support structures must be designed to withstand the force experienced by the part. The support structures are designed as an array of struts uniformly distributed across the projected print area. The struts are designed with a set radius r_{strut}, and a number of struts, n_{strut}, actively holding up a newly cured layer. These parameters can be combined to achieve a total area of support material as expressed in equation 4.1.

$$A_{supp} = \pi {r_{strut}}^2 * n_{strut} \quad \text{eq 4.1}$$

Since the print area of a given layer will change layer-to layer, it is only be assumed that the engaged struts are those normal to the suction force F_{print}. Thus, n_{strut} is dependent on a selected strut density, ρ_{strut}, which is the number of struts per mm^2 as defined by the projected area, A_{print} of the current layer. This dependance on strut density results in a varying number of struts as the curved element expands or shrinks in print area as seen by equation 4.2.

$$n_{strut} = \lceil A_{print} * \rho_{strut} \rceil \quad \text{eq 4.2}$$

Where the n struts are uniformly distributed across the area of the total projected area and ⌈ ⌉ represents the ceiling function which rounds the strut number rounded up to the nearest integer. These defined support parameters inform are combined with the fracture stress of the cured resin to calculate the force withstood by the support structures, F_{supp}.

- $F_{supp} = \sigma_m * A_{supp}$ eq 4.3

Equations 4.1, 4.2, and 4.3 are combined to determine the total force withstood by the support structures seen in equation 4.4

$$F_{supp} = \sigma_m * \pi {r_{strut}}^2 * \lceil A_{print} * \rho_{strut} \rceil \quad \text{eq 4.4}$$

4.1.3. Printed Element Parameters

In the design of latticed and freeform transducers, two element types were to be printed: a latticed element and a curved disk (freeform) element. While the thin-strutted lattice structures maintained a low strut radius, resulting in low surface area layer-to-layer and easy printability, the printing of the 15mm curved disk element posed a much more difficult problem.

For the curved elements printed in these experiments, the print area, A_{print}, is described in Figure 15 wherein the print is reduced to 10 layers for the simplification of the relationship.

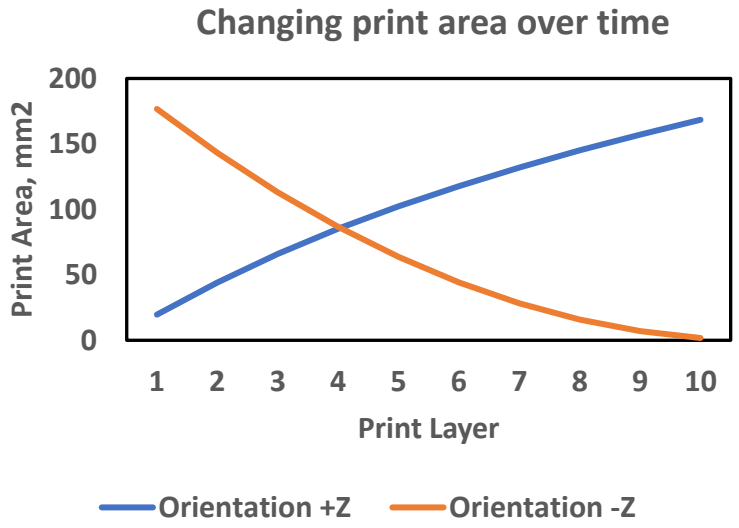

Figure 15. Print area as a function of print radius. +Z orientation is the curved element has the back of the curve to the print stage such that the print area increases with each layer. The -Z orientation is such that the area decreases with each layer.

Designing the strut generation to withstand such a load imposed by the area defined by the print layers requires a calculation of max allowable force, or the max F_{print}. Stefan's adhesion as expressed above is used to define the max F_{print}, given the following parameters: The resin composition used in the present experimentation is 35vol% PZT with 65vol% PEGDA. This has a viscosity similar to other materials tested in the lab, 7.8029 Pa*s (20%vol CFRP resin). Using these viscous properties, the suction force during the lifting of the motion stage was calculated.

The height of separation, h, is equal to the dead zone height formed through the use of an oxygen-permeable print window, which is generally in the range of ~2.5μm according to [37]. Poor airflow to the PDMS film and high particle loading may have reduced this further than the considered h=2.5μm. A constant stage velocity was set at 15mm/s in the z direction, and a radius of the curved disk reached its maximum at 7.5mm. Through this, the upper limit of force experienced by the print is calculated to be 111.6 MN.

Recognizing the need to match this force loading, the strut parameters are calculated. By reordering formula equation 4.4 and selecting a strut density of 0.2 as a starting point, we calculate the radius necessary to withstand the maximum F_{print}. This occurs at the max print area, $A_{print} = \pi {r_{print}}^2$. Wherein r_{print} is the same r from the Stefan Adhesion equation equal to 7.5mm. Since the particle-loaded resin is structurally held together by the curing of the photopolymer matrix, the fracture stress, σ_m, is defined as the fracture stress of the PEGDA matrix as defined in literature: 25-35MPa [33] The resulting initial support strut radius is defined to be 0.2mm.

Initial tests for printability are carried out on the curved transducer element: The element is concave, producing layers that move from a radius of approximately 0 to 7.5 mm. The final element tested is 1 mm thick. The element was tested in 2 orientations: +Z concave towards the vat) and -Z (concave towards the print stage). This is more easily understood in Figure 16.

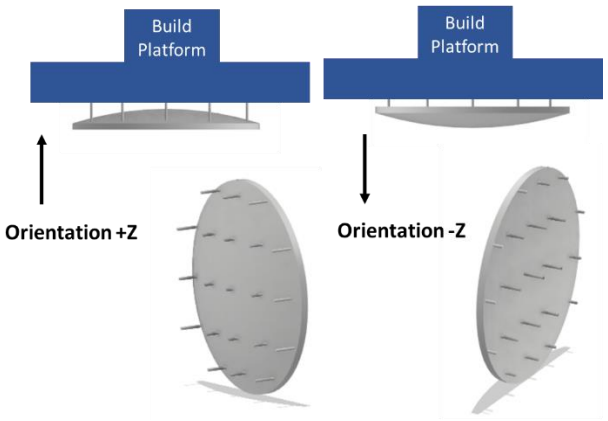

Figure 16. 2 orientations of the curved element. (left) print orientation +Z, (right) print orientation -Z.

As observed, Support material connects the element in its two orientations to the bed, allowing a 2mm clearance for a blade to separate the part from the stage. 2 flat layers of PEGDA followed by a PZT-loaded resin layer are cured as the first 3 layers, enabling a strong bond to the print stage. Exposure times are gradually increased in each of the two orientations, considering the differences in behavior between orientations and at differing UV dosages. This accounts for the reduced depth of penetration, enabling observation of the point of print success.

4.1.4. Strut Redesign

Informed by initial testing, a refined print model is then proposed and tested to improve printing success by factoring involving both exposure time and PDMS window wear by layer. An additional set of terms are combined with the Stefan Adhesion model above to realize the print force experienced by the part. These terms consider influences affecting the reduction of the deadzone, h. Kumwar demonstrates tests which appear to demonstrate a decay of deadzone size at a rate exponentially related to exposure time, T [38]. The experimental results of Kumwar are interpreted as demonstrating the following relationship:

$$h \sim h_0 e^{-\alpha T} \quad 4.5$$

wherein h_0 is the initial dead zone, T is exposure time of a layer, and α is a coefficient defined by the print context (ie. properties of the resin, PDMS window, oxygen flow to the window, etc). A second term is added into the model based on the cyclical loading from compression and suction forces imposed on the PDMS window from elevator movement [40]. Term included for PDMS wear is combined in terms of layer number, l. This expands on the term observed in equation 4.5, as the greater time of exposure experienced at a given layer, the greater the force experienced by the print and the greater the wear on the PDMS. Thus, T and l have a compounding effect as seen in the terms expressed through equation 4.6.

$$h \sim h_0 \, e^{-\alpha T l} \tag{4.6}$$

In this case, α is modified to additionally encompass the mechanical properties of the PDMS window (ie. Yield stress, Crack propagation, etc) and even the resin. To balance units, α is also defined by the units $(\text{seconds-layers})^{-1}$.

The term in equation 4.6 is combined with the Stefan Adhesion equation to yield the proposed force model for a printed part at exposure time T and at layer number, l.

$$F_{print} \sim \frac{3\pi\mu u r^4}{2{h_0}^3 e^{-\alpha T l}} \tag{4.7}$$

To modify the struts for the increased force experienced by the support struts, the strut density is divided by 2 and the radius of the support struts is multiplied by two. Considering this modification in the context of equation 4.4 reveals an overall increase in strut force by a factor of $2^2/2 = 2$. The modified strut orientation is tested at the same parameters as described in the initial test, wherein the orientation is set to +Z and -Z while each has its exposure time gradually increased.

Experimental results are analysed and compared to the behaviors demonstrated by theoretical plots of the model at various T values and for the two strut designs. The findings are discussed in following sections.

4.1.5. Results

The resulting strut designs for initial print tests were generated using the parameters defined in methods: strut density = 0.2 and calculated strut radius of 0.2mm. The resulting force, considering n rounded up to ensure a greater force was 111.7MN. The struts were successfully distributed in a concentric and uniform manner to the designed curved piezo element in both orientations: +Z and -Z.

Despite intentional design to withstand loading from the print force using Stefan's adhesion, the resulting prints all produced failure in one of two modes. Failure occurred as expected at the struts or unexpectedly near the final layers of the print as seen in Figure 17.

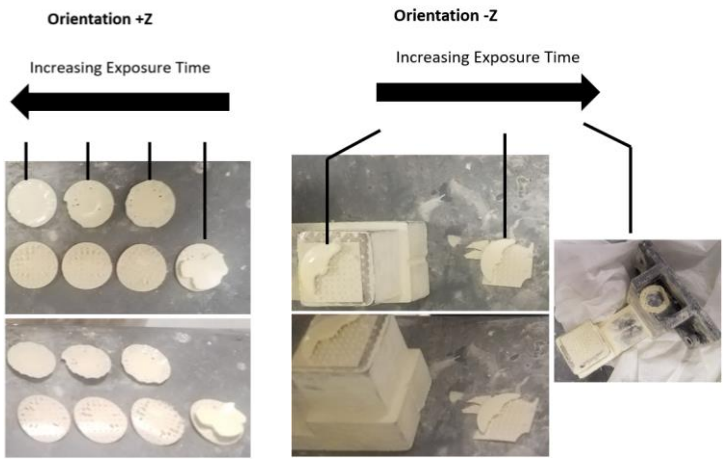

Figure 17. Initial Curved element print trials with struts calculated based on Stefan Adhesion model. (Left) +Z orientation print trials increasing in exposure time, T, from right to left. (right) -Z orientation print attempts increasing T left to right.

To describe the behavior, a biproduct of the prints was considered: the post-print PDMS window. 0 reveals PDMS wear of variable amounts. While the windows used in this experiment were not photographed, Figure 18 demonstrates the same phenomena observed during printing.

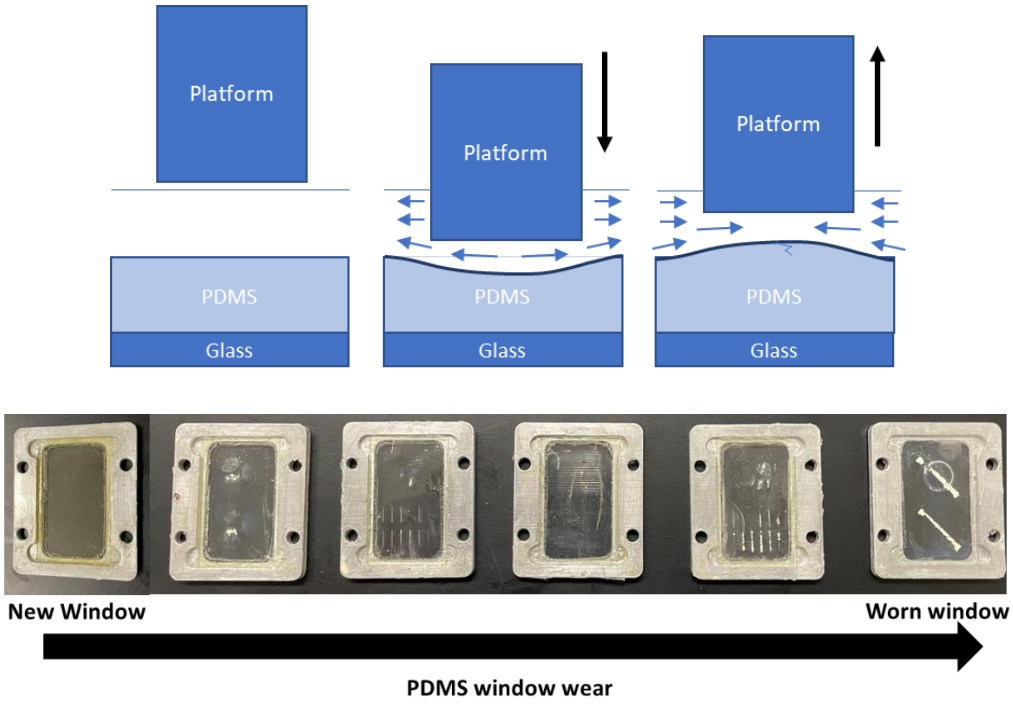

Figure 18. (top) Cyclical loading of compression/suction subjecting PDMS windows to wear after each layer is represented and (bottom) variable wear on PDMS windows is shown (presented photograph by H. Liu does not show windows from alternate lab trials outside of this work)

The wear of the PDMS window as a result of use with slurry-based printing is shown. To validate the observed print attempts, proposed model of the expanded Stefan adhesion equation, as applied to SLA, is plotted as the resulting force against the initially designed support structures and shown in Figure 19.

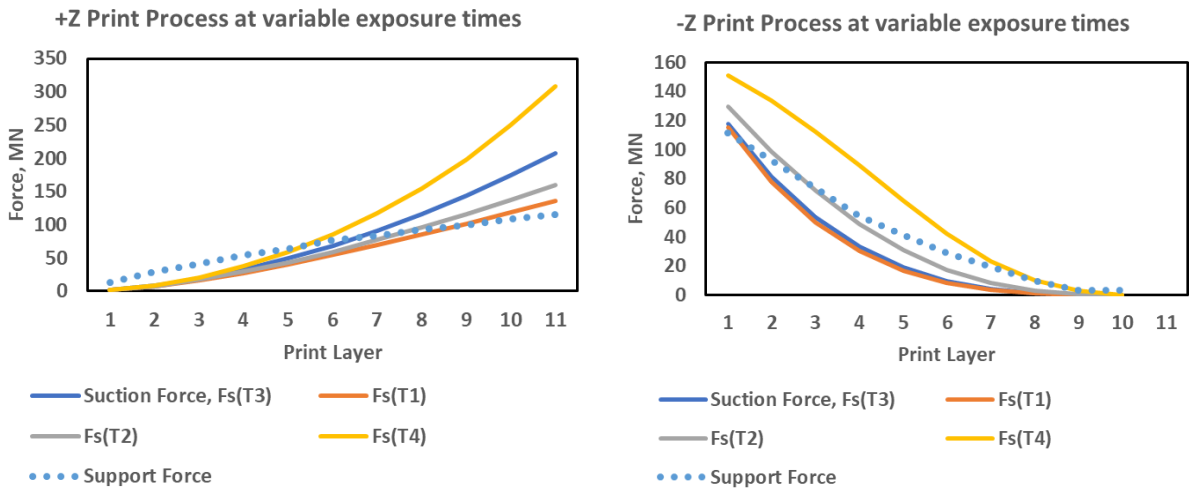

Figure 19. Initial Print Trials. Support force plotted with Suction force, Fs in MN at increasing exposure times, calculated according to the proposed equation 4.7. Fs1 is the lowest T and Fs3 is the highest T. Intersection of support force and suction force results in the failure of a print as seen in (left) +Z orientation with increasing print area (right) +Z orientation with decreasing print area. Strut density: 0.2; Strut radius 0.2 mm

In each trial, the print force, F surpasses the support force, validating the behavior we observed during experimentation.

To accommodate for the increase in force experienced by the support structures at later layer counts, the radius of the support struts was multiplied by a factor of 2 and the density was divided by 2. The output strut design is plotted against the expected forces according to the new model, and the output is shown in Figure 20.

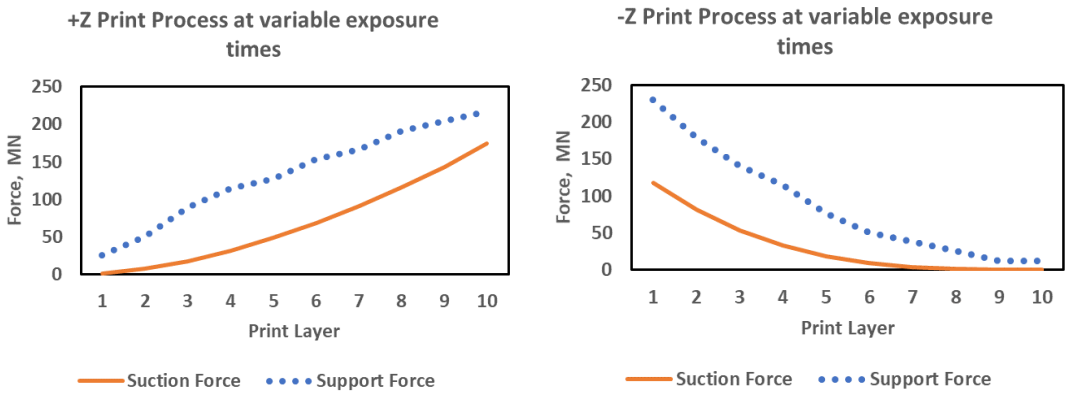

Figure 20. Redesigned Print Trials. Support force plotted with Suction force (MN), calculated according to the proposed equation 4.7. The lack of intersection of support force and suction force implies a successful print (left) +Z orientation with increasing print area (right) +Z orientation with decreasing print area. Strut density: 0.1; Strut radius 0.4 mm

The resulting projections at a constant exposure time of 1.8 seconds appeared to be successful relative to previously tested prints.

The new strut design is implemented into the element and printed. This increased support force enables the support strength to remain greater than the suction force, despite increased force experienced from the dead zone over time and layer count.

This projected success is validated through the successful printing of the transducer element shown in Figure 21.

Figure 21. Successful HIFU transducer element. Low support density, optimized print time, orientation -Z.

Successful prints were also carried out for the +Z orientation, however these prints were not photographed before post-processing.

4.1.6. Discussion

For strut design, the strut model provides a method to calculate strut thickness. This can be defined by selecting either a strut radius or strut density. Limitations and opportunities for improvement in this method are the need for struts to be manually placed on the part. With struts distributed in such a way where distances are both uniform and connect to key points on the structure such as the lowest point of the curve and outermost edged of the disk. This may require secondary decision making and manual intervention to ensure an effective distribution.

For initial testing, the tests of the designed struts for printing failed as shown in Figure 17. When considering additional factors in equation 4.7, as shown in 0, the behavior observed is validated. The behaviors demonstrated by the +Z orientation are such that failure occurs progressively throughout the print at different times.

Referencing the +Z print attempts in Figure 17 (left), we can see the printed element close to success, followed by progressive failures earlier in the print process. This is the same behavior demonstrated by the model plotted in Figure 19 (left), wherein the marginal increases in exposure time result in a reduced dead zone which yields greater forces applied to the part. Even when the part reaches near-completion on the right-most +Z trial, the mechanical wear on the PDMS window results in failure at the edges of the part. Final suction forces are greater than the allowable forces of the supporting structures in locally worn regions. Model in 0 demonstrates how this surpassing of print force onsets earlier at higher exposure times due to the reduced deadzone. Exposure values lower than those displayed were too low to reach the critical exposure, resulting in the failure to even produce support struts.

Unaddressed in the printing of this element with regards to the model is that the radius rises over time, without parameterization of an inner radius at later layers to create an empty circle. This shape has an obvious reduction in surface area which may be believed to reduce the suction force contrary to the model's prediction. This is considered in two ways to affirm the model. Firstly, the model assumes constant density of struts, which shall enable a scaling of the forces felt in correlation with the subjected print area. In this regard, the additional predicted area is offset by the presence of acting struts maintaining a balance in both forces aligned with the expected behavior. The second consideration is that the suction force will remain relatively constant regardless of the present gap in the +Z orientation, since the space within the inner radius is enclosed. The enclosed space of the element will trap air or resin in the curvature of the element, requiring the element to pull additional resin under while lifting the print stage. This present suction force may additionally apply forces to the inside of the curvature which could lead to the element caving in.

This second consideration is believed to influence the ripping of the element as observed on the right of the +Z orientation in Figure 17 After the trapped fluid or air is relieved, the suction force is alleviated, stopping the rip from propagating throughout the entire element as seen in the -Z orientation on the left of Figure 17 (right).

The -Z orientation shows failure in one of two modes: at the very beginning and at the very end. Looking to the model graphed in Figure 19 (right), the two locations of potential failure are determined to be either the very beginning of the print or the end of the print. Considering the parameters of the model, the beginning failure mode exists because the max print radius, 7.5mm, is present on layer 1 of the print. This is clearly observed in Reductions in cross-sectional print area throughout the entire print reduce force loads comparatively until late in the print at which

point only few support struts remain normal to the area being printed. The cumulative PDMS wear amplifies forces applied to the small print area. When the suction forces exceed those, which can be supported by the active struts, fractures occur, and the part is ripped apart as shown on the left of Figure 17 (right). When exposure times are reduced beyond those shown in the print attempts, the struts are not cured, resulting in a failed print.

For updated tests, by doubling the strut radius and dividing the strut density by 2, the support area of the struts is scaled by a factor of 2. This scaling by 2 displayed allowable forces safely above those projected by the model as seen in of Figure 20. Printing these elements yielded successful part manufacturing as shown in Figure 21. While the struts were thicker as a result, the reduced density localized progressive PDMS wear, potentially assisting in the print success. The thickening of the struts introduces a need for deeper care while strut removal, as holes may be left on the elements at the location of strut removal. This is a trade-off that comes at the cost of more struts being removed and potentially greater wear to the PDMS window. Ultimately, printability is the core concern, and this was achieved by enabling a designed support structure projected to withstand forces of suction produced during printing, accounting for negative effects of increasing exposure time and cyclical wear to the print window.

4.1.7. Additional considerations of the process and materials

Other prominent limitations unaddressed in this work are a need for variable exposure time and degradation resulting from resin lifetime.

Energy arrives at the resin surface in a gaussian distribution, so the projection method of the DMD, a series of pixels displayed as a mask on the screen, results in reduced exposure on edges of the projected mask relative to the enclosed projection areas. This reduced edge exposure does not play a prominent role in the printing of thin-strutted structures such as those used in the

hydrophone design, however the printing of as solid form introduces complications to the printing process. These complications are overcome by a different exposure time applied to the struts than that which is applied to the printed part. This modification is not considered in the model, since the printing rate of the part was held constant after reaching the part. This behavior of improved curing at larger enclosed areas may have additionally contributed to the success of the second support strut design. In doubling the radius of the support struts, the layer-to layer tensile strength may have been improved.

The second consideration unaddressed is resin lifetime. When a resin is mixed, its effectiveness begins to degrade, becoming less receptive to UV light over time. Since the tests run on the various trials were carried out at different times after mixing of resin batches, the precise times of exposure will not have the same response. This is addressed through the gradual increase of exposure time, revealing trends independent of specific exposure times.

Overall, the model is presented to be useful in realizing the behaviors of exposure time and layer count on forces experienced by the printed part and its support struts via reductions in the dead zone.

4.2. Element Post-Processing

After understanding print parameters, piezoelectric elements were printed for each of the six designed lattice variants. Since the green prints retain support material, and the ceramic elements are still held together merely with the photopolymer matrix, post processing must take place.

4.2.1. Refining Green Parts

The samples were rinsed with ethanol, but since the photopolymer was to be removed during the sintering phase, post curing was not used on the samples. At this stage, the samples are still slightly malleable; care while handling is necessary.

Unnecessary support material is carefully removed from the element, and sanding ensures a smooth surface finish as seen in Figure 22.

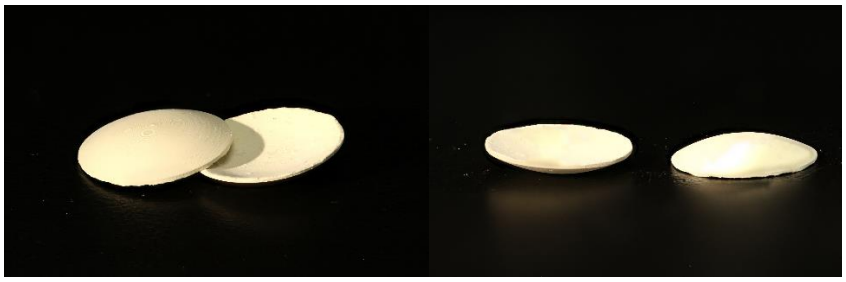

Figure 22. Post Processed HIFU transducer element

4.2.2. Sintering

The green samples are placed in a crucible that is filled with lead particles to prevent the loss of lead in the processed part during high temperature exposures.

The part is heated to 400C in 12 hours, held there for 1 hour, increased to 1050C in 2.5 hours, held there for 1 hour, and returned to room temperature gradually (3.5 hours). Increasing the sinter temperature above 1050 C would exceed the critical temperature of the PZT, resulting in discoloration and significant reductions in performance.

The sintering cycle burns out the photopolymer resin matrix while the leftover PZT undergoes densification [46]. During this process, the elements undergo ~50% reduction in size and slight deformations from their green state. These changes vary between samples, requiring a measurement step discussed in the case design. Scanning is an alternative method of analysis to inform case dimensions for the hydrophone elements or other forms which are more complex. The

Sintered transducer elements are shown in Figure 23 to have discoloration resulting from the removal of the resin matrix during sintering.

Figure 23. Sintered HIFU Transducer element

4.2.3. Poling

The Sintered elements were poled using 30KV passed through a copper electrode under the element, and into a metal probe above the element. 3M™ Fluorinert™ Electronic Liquid (FC-3283) is a nonconductive and thermally stable fluid which was used to enable poling through the PZT despite the latticed structure [16]. The specific method used here is called Corona poling; it has previously been applied to other additively manufactured sensors[13].

The 30kV electric field was applied for 1 hour, making the sintered lattices responsive in the poled dimension.

4.2.4. Case Printing

With the elements sintered appropriately, measurements were made to dimension the bounding volume from which transducer cases were generated. Cases were printed on the AnyCubic Photon printer out of resin from PEGDA and Sudan mixed in the lab.

4.3. Subcomponent Assembly

With all materials present, elements printed/sintered/poled, and cases printed, the hydrophones were assembled. This process takes place from the innermost component, out. Reference to 0 provides a visual as applied to the hydrophone application. The HIFU medical application is also

assembled. The processes, while translatable across application, are broken down into separate sections.

4.3.1. Hydrophone

Since the print model expressed for the curved disc elements were more complex than those of the hydrophone, the printing of hydrophone element was simple.

Initially, the elements are secured into the casing in a series connection: element-electrodes-casing. The element is secured to the interior walls of the case via electrode paint. This was carried out by applying the conductive silver paint to, acting as electrodes, to opposite interior walls of the case before element insertion. The tolerancing of the case applied minimal friction on one to three struts, holding the element in place, however inconsistencies from sintering prevented full wall-contact from all struts. To ensure electrode connectivity to all struts of the piezoelectric lattice element, the paint was applied with 0.5mm thickness. This tolerancing of paint from the wall enabled contact from all struts, forming the positive and negative electrode faces. Before drying, 0.01mm copper wire was also inserted into the paint to enable access to the electrodes once the casing was sealed. While the silver paint solved the tolerancing problem for the sintered elements, it was later hypothesized that the brittleness of the dried paint influenced cracking and loss of responsiveness during transducer handling and use.

Before the paint dried, the square elements were slid into the casing, oriented such that the poled axis of the element is normal to the painted electrode faces, contacting them on the top and bottom of the poling.

Castor oil was used to fill empty space in the case, including the gaps between lattice struts. This eliminated the air in the casing, so to ensure no air was trapped, the oil-filled casing and element was placed in a vacuum and subjected to an ambient pressure of -100kPa, forcing any

trapped air bubbles to shrink and rise out of the casing. This additionally forced oil to seep from any cracks in the casing. The oil was topped off to ensure no air would be trapped in the casing; any air will result in large reflections from the acoustic waves. The Lid of the casing was sealed onto the case using manually applied PEGDA, selectively cured with a UV flashlight.

In the case of the hydrophone, electromagnetic shielding was necessary to prevent electromagnetic interference carried by the water. The shielding was applied by contouring a conductive tape mesh to the case. While a secondary case was applied to maintain the shielding mesh, it was later deemed unnecessary as the shielding would be maintained in place by a waterproofing agent. The tape was connected to the ground wire of the coax cable and the ground electrode. The positive electrode was soldered to the positive signal wire in the center of the coax cable. This was sealed to the case to prevent excess vibrations.

The shielding was wrapped up the wire as seen in Figure 24 before being submerged in transparent liquid electrical tape for waterproofing. The internal casing with element and electrodes is seen with the finalized transducer in Figure 24.

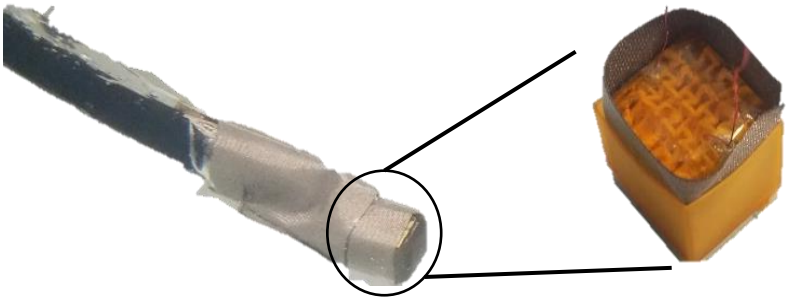

Figure 24. encased transducer connected, wrapped, and sealed.

4.3.2. HIFU Transducer

The HIFU transducer was manufactured using a similar process as the hydrophone. The casing design and assembly technique for this transducer is adapted from a process used in Dr. Eli Vlaisavljevich's Therapeutic Ultrasound and Non-Invasive Therapies Laboratory, with alternate materials more available to the Additive Manufacturing Metamaterials Lab (AMML) [78]. In this case, quick setting epoxy and was used in place of the castor oil; the epoxy will act as a backing layer, limiting reflections out the back of the transducer. Due to the brittleness experienced by the conductive silver paint, a highly conductive silver epoxy was applied as the electrode. The high viscosity of the epoxy made application onto the element directly simpler and more reliable. The application of the first electrode is shown in Figure 25 (top left image). The connected element is pressed into a thin layer of epoxy which has been placed in the casing. The compression spreads the epoxy across the element face, covering the entire surface. Gaps around the rim allow excess material to flow up without wrapping around the element or maintaining air gaps between the emitting element and the transmission layer. At this point, the connection is additionally tested to confirm all electrodes are appropriately placed. With all electrodes in place, the quick setting epoxy is injected into the backing to fill the case, before being left to set in a clamp. Labelled wires from the electrodes are fed through a hole in the back of the case.

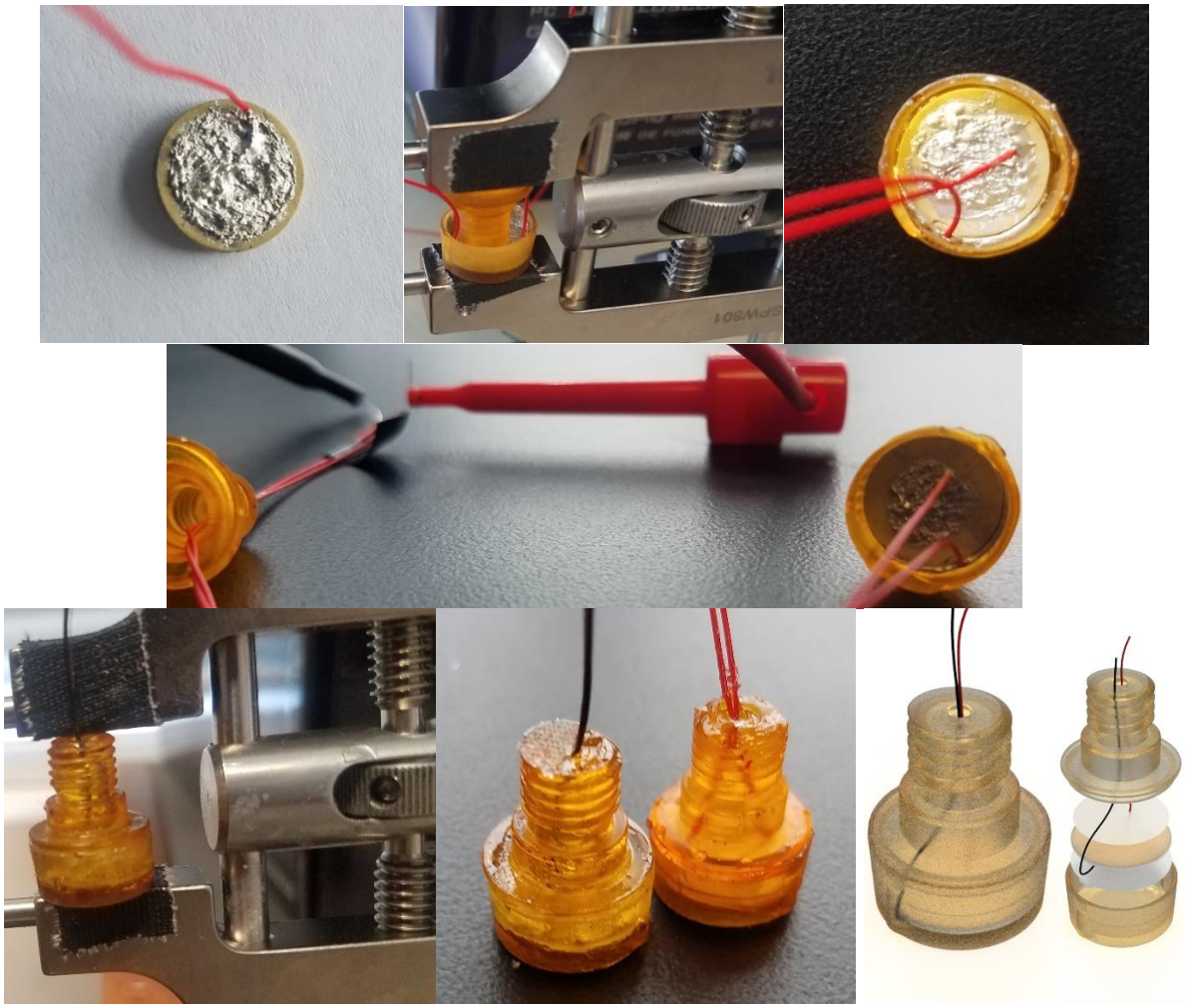

Figure 25. Transducer Assembly process from (top) painting and compressing of silver epoxy electrode to (Bottom) Sealing of casing and backing material. (bottom-right) Render of assembly subcomponents.

Chapter 5: Independent Element Testing

With lattice elements and transducers fully assembled, the latticed hydrophone must be tested to confirm the novel tunability of response amplitude and frequency range. Tested elements are selected throughout the tunable frequency range and sensitivity range outlined in Chapter 2. In order to carry out testing of the expected responses, decisions on measurement and fixturing design was required. In this chapter setup expresses these decisions with their rationale followed by testing methods, results, and discussions. A brief review of the lattices being tested is also included.

5.1. Lattices Tested

The hydrophones tested are hypothesized to demonstrate tunability of operating range (a function of peak resonance) and improved responsiveness under the assumption that the composite oil-PZT transducer element will have reduced acoustic impedance, mitigating acoustic reflections.

Three screw angles were selected, using the lattice geometry outlined in chapters 1 and 3: 75, 90, and 120. These three structures were additionally generated at two relative densities by varying strut thickness and strut length for each geometry. These relative densities are referenced to as "high density" (H) or "low density" (L) Altogether, this generated 6 lattices named in a convention of (XX) wherein the first letter represents density and the second represents angle theta. An example of this is the "High density, Auxetic" (HA) lattice or the "low density Honeycomb" (LH) lattice. The Lattices are also referred to in figures with reference to the screw angle, θ, and the relative density wherein low is $\bar{\rho}$ =15% and high is 27%.

5.2. Setup

To test the hydrophone performance and evaluate the predicted performance, A controlled testing environment was necessary. Two testing tanks were developed: an initial "small tank," and

a “large tank.” More effective testing was completed in the large tank due to resonant modes produced in the small tank influencing high fluctuations in amplitude readouts. Before any tanks or mounting setups were developed, however the electrical and hydroacoustic systems must be established to generate underwater sound at various controlled frequencies and to read in the electrical signals produced by the hydrophone.

5.2.1. Electronics

The electronic systems are presented in a collaged overview through Figure 26.

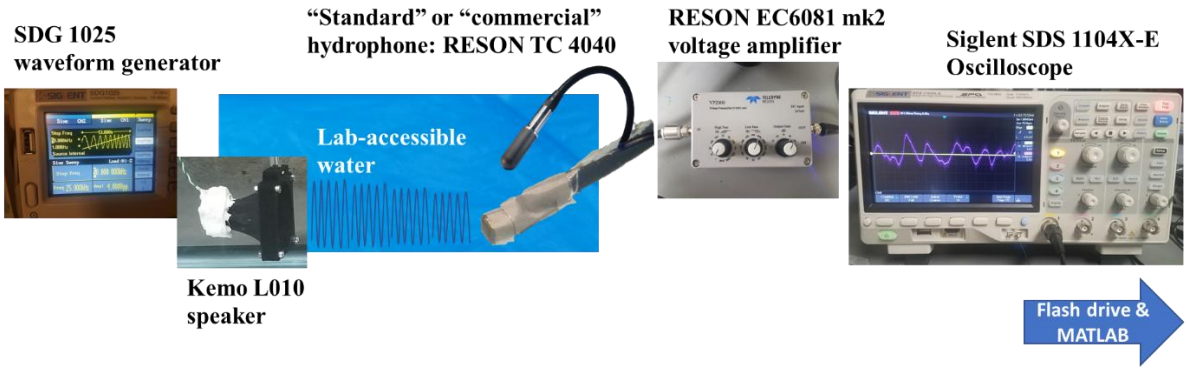

Figure 26. Flow of energy from the electronic systems through to data processing. The electrical wave is emitted from the signal generator and converted to ultrasound via the speaker. Sound propagates through the water to the experimental of commercial hydrophone where the amplifier augments the signal and passes it to the oscilloscope. The resulting signal is analyzed in MATLAB.

Signal Generator—The SDG 1025 waveform generator, capable of 25MHz, was used to produce the electrical waveforms passed into a speaker. Various tests were run including sweeps and stepped frequency tests ranging from 1KHz to 60KHz.

Speaker—The speaker is a Kemo L010 in-air speaker piezoelectric that has been sealed with silicone. The vibrations of the speaker introduce cracks in the silicone seal, so speakers only have a brief testing life before a new speaker is needed. While the silicone is not uniformly applied to the speaker which may have influences deformations to the acoustic signal, the silicone does

demonstrate material properties which may assist in impedance matching to help reduce reflected emissions of the speaker. Any deformations in sound were determined to be negligible upon initial tests reading expected values from the standard hydrophone.

Lab-accessible water—The water used in the experiment is provided by the lab via lab sink. Virginia tap water does not have a salt content comparable to the ocean which is the intended use of the hydrophones. Nevertheless, water as a medium for acoustic transmission and attenuation was controlled for in its use in all tanks for the purpose of piezoelectric lattice element experimentation.

Standard Hydrophone—A RESON TC 4040 hydrophone from Teledyne was used as a standard hydrophone for comparison to our hydrophone. The hydrophone has a water-resistant rubber cylinder, filled with a transmission oil, and its core is a ceramic piezoelectric disk.

Amplifier—The RESON EC6081 mk2 voltage amplifier from Teledyne was used to apply gain to the hydrophone outputs, achieving a readable level. The preamplifier was set to a gain of 40 dB after observing a drop-off in performance from the amplifier at high frequencies when set to the 50dB gain setting. A lowpass filter was set to 100KHz on the preamplifier, and a high pass filter was left at 1Hz. While the preamplifier was designed to boost the signal with a built-in battery, the signal would drop off mid-test due to low battery power. For this reason, a 24 volt power supply was connected to the preamplifier during all tests. The presence of the preamplifier immediately applying a gain to each hydrophone signal eliminated the need for a circuit setup to amplify the piezoelectric readout. The preamplifier was directly connected to the oscilloscope via coax cable. The additional 40dB gain is considered in the processing of the data outputs by simply subtracting 40 from the sensitivity output.

Oscilloscope—A Siglent SDS 1104X-E Oscilloscope was used to read in the signal from the preamplifier that are amplified from the piezoelectric element are read in at the oscilloscope. The instrument was set at a sampling rate of 1-2Msamples/second, outputting 14.0Mpoints. The output points are loaded to a flashdrive to be processed in Matlab. RMS voltage setting was also used on constant frequency measurements to manually record voltage readings at a resolution of 250microvolts.

5.2.2. Test Tank Selection

The tank selection for testing was a critical element, as it is a defining feature of the measurement system. A small tank was initially used for fast results, revealing two major considerations: resonance in the tank and far-field considerations. This resulted in a final selection of a larger tank for testing. Lastly, fixturing is generated for the tanks.

5.2.2.1. Small Tank

Through early testing, and hydrophone handling, lessons were learned to inform the final testing tank. The Main concerns to surface are a tank large enough to exceed the Far Field of the acoustic source [7] and tank resonance frequencies due to tank geometry and tank size [85]. The initial tank used is rectangular as shown in Figure 27 a fixture was designed and printed for mounting in this tank in attempts to achieve consistent measurements.

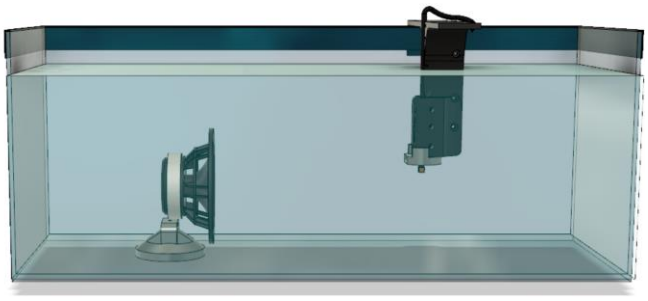

Figure 27. Small testing tank and mounted speaker/hydrophone

In the small tank, small movements in the speaker played a significant role in causing variability in the signal. For this reason, the speaker was adhered to the base of the dry tank with fast-curing epoxy before being filled. This permanent mount point significantly reduced inconsistencies in data recorded, as any contact with the wire or vibrations during emission of signal would create erroneous fluctuation in the readout.

5.2.2.2. Tank Resonance

Duncan (2016) demonstrates the effects of tank resonance on pressure fields generated from an acoustic source in various tank shapes and at various frequencies[85]. The effects of such fields influence significant special pressure differences resulting in large measurement changes from marginal shift in the position of a hydrophone. Similarly, pressure differences occur over a frequency sweep when a receiving element remains stationary. The size and geometry of a tank modify the resonant frequencies, and our initial tests demonstrated that the smaller tank yielded extreme variability with respect to minor positional changes. Jones (2019) expresses that "Reverberation by tank boundaries is inevitable to some extent." [65], so the best that could be hoped for was to achieve a large enough tank to diffuse reverberations to a level comparable to noise. Additionally, the tank geometry was selected in an effort to minimize reflections to the element. A large circular tank would limit reflections to the central point where the hydrophone was to be tested, and shifts in the positioning of the hydrophone would result in a constant amount of reflection enabling consistency across measurements [85].

5.2.2.3. Far-Field Considerations

In addition to the generation of modal amplitude fluctuations, the far field was additionally considered as a future impacting factor on the data quality collected from initial small tank testing.

The far field, r, is the radius surrounding an underwater transducer within which acoustic amplitude is non-linearly related to the distance, x from the transducer.

$$r = A/\lambda \qquad \text{eq 5.2}$$

Where A is the largest active dimension of the transducer element and λ is the wavelength emitted or received. This nonlinear behavior is a function of the constructive and destructive wave interactions generated by the outer edge and the center of a piezoelectric disk as it oscillates. Applying equation 5.2 to the Kemo L010 speaker with a 1cm radius circular piezoelectric element, and assuming the highest testing frequency at 5MHz, we determine a far field of 1.1m.

Operating within the far field yields chaotic results, as a very small shift in the placement of the hydrophone being tested will produce dramatically different results.

5.2.2.4. Large Tank

A circular constructable swimming pool was selected as the large testing tank for its large size, circular form, easy/rapid assembly, and low cost. The selected “large tank” allows for consistency of measurement amid minor movements of the hydrophone, thus allowing for measurement of two closely located hydrophones (such as a sample and reference) The large tank additionally insures measurement capacity beyond far-field limitations. The large tank is dimensioned in Figure 28 with other setup components additionally diagrammed.

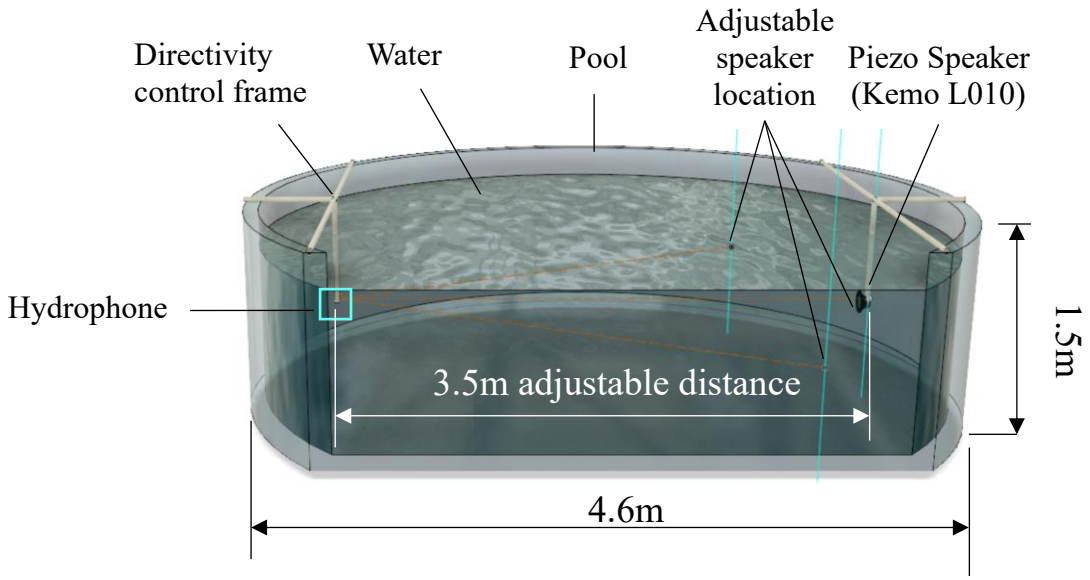

Figure 28. Large Testing Tank and mounted speaker/hydrophone

Minor movements or vibrations in the fixturing were not of concern in the large tank, as there was reduced noticeable acoustic resonance forming in the tank. For this reason, the fixturing of the large tank was constructed from PVC piping, enabling low cost, quick construction of the fixture. A clear gradient, seen in Figure 29, could be observed by moving the speaker closer or further from the hydrophone.

This signal shown in Figure 29 reveals the amplitude resulting from an 8kHz input signal to the speaker read out by a hydrophone in the time domain from two set distances 1 meter apart. Confounding signals from reflections off the tank wall appear to be relatively low with clearly higher amplitude at the closer distance. An FFT of the signal not shown here confirms that this 8kHz frequency dominates the signal, thus supporting the test in achieving the intended outcome of observing changes in the signal.

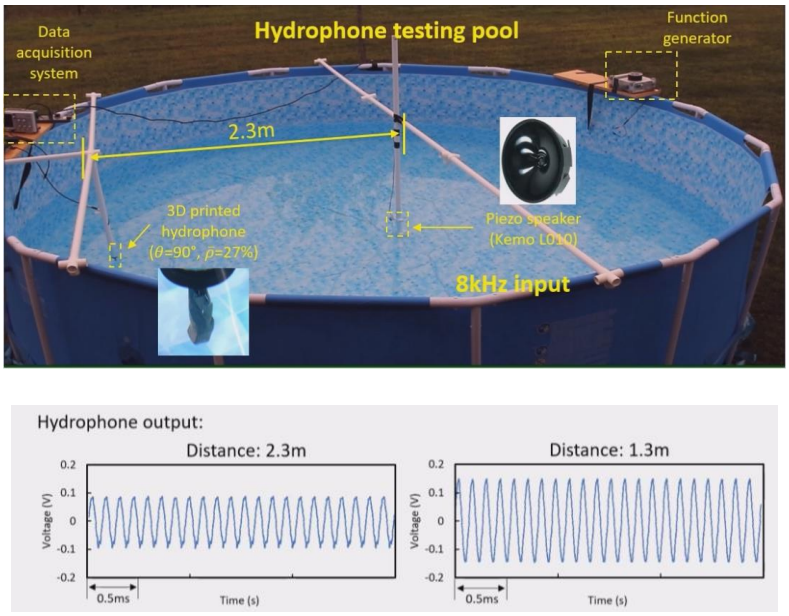

Figure 29. Large tank (top) live setup and (bottom) distance validation signal output via an 8kHz signal at two set distances; greater signal amplitude is clearly observed at the closer of the distances

During the actual testing of the elements, FFTs are used to record only the emitted signal frequency. The soft walls of the tank dampen reflections, making reflected effects on the output signal negligible. Additionally, the careful placement of samples in the same location and mirroring location across the centerline of the emitted signal still enables the relative sensitivity to be compared between samples. This informs the potential for tunability which is sought through this work.

5.2.2.5. Mounting

The mounting points in both tanks were designed to maintain the hydrophone in a specific and consistent location. This was particularly important in the small tank, as the tank resonance produced peaks in amplitude directly adjacent to low amplitude regions [85]. In addition to this need, the fixture was designed to be minimally obstructive of the acoustic field experienced by the hydrophone and housed both the standard hydrophone (12mm cable with 26mm diameter cylinder attached) and the latticed hydrophones (6mm diameter cable with 7 mm cube attached).

The fixture in Figure 29 was used to maintain constant distance from the bottom of the tank, 0.5m, and a constant distance between the speaker and hydrophone being tested, 3.5m. marks on the rim of the pool were made as well as marks on the PVC piping to ensure accurate placement on every trial. The speaker positioning was adjustable to ensure a correlated change in amplitude could be observed by moving the speaker closer or further from the tested sample. The wires of the systems were fed up the PVC piping, and into the instrumentation (ie. Waveform generator, preamp, and oscilloscope). Instrumentation was maintained safely near the edge of the tank.

5.3. Independent Element Testing Methods

After refinement of setup, each of the lattices outlined in section 3.2.1. , the standard hydrophone, and a PVDF Film for benchmarking were initially tested in the large tank at a frequency of 7kHz. The hydrophones were tested simultaneously against the standard hydrophone which remained static, mirroring the position of the latticed hydrophone across the centerline in the direction of sound propagation as seen in Figure 30. This mirroring mitigated any effects of resonance in the pool, as the symmetry would apply the resonance equally.

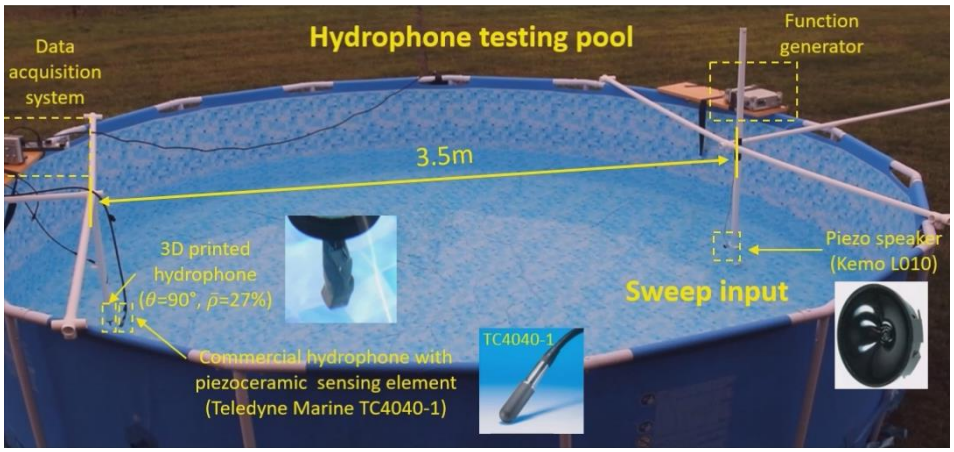

Figure 30. Experimental Test setup

Of the tests carried out, the most reliable hydrophone samples, demonstrating the most effective construction and lowest noise from loose electrode connections, were further tested against the specific sensitivities read out by the standard hydrophone and PVDF film.

The experimental signals were processed in Matlab, using the voltage output of the standard hydrophone to project the acoustic pressure, p_0, at the hydrophone location [7].

$$p_0 = \frac{V_{std}}{10^{\frac{M_{std}+120}{20}}} \qquad \text{[eq 3.3.1]}$$

Where M_{std} is the known sensitivity of the standard hydrophone. Applying the measured pressure to the readout of the tested hydrophones, we evaluate the sensitivity, M_h, of the control and latticed hydrophones [7].

- $M_h = 20 \log\left(\frac{V_h}{p_0}\right) - 120$ [eq 3.3.2]

Where V_h is the hydrophone's Voltage output as read out through the oscilloscope. The amplifier setting and distance travelled are kept constant during the measurements, maintaining the pressure level at the location of hydrophone constant during all trials.

In addition to the constant frequency tests, a sweep was applied to the experimental hydrophones over a range of frequencies from 1kHz to 30kHz. For some lattices this was extended to 60kHz. The outputs from the frequency sweep were transformed into sensitivity using equation 3.3.2 in order to observe the working range of the hydrophone. The working range is quantitatively determined via processing of the frequency sweep via Matlab with an FFT; noise is manually removed to reveal a clear frequency peak amplitude of frequency, which is determined to be the resonance point. The cubic lattices were measured against the standard hydrophone and control PVDF and PZT elements; final testing results were plotted and compared for sensitivity and working range.

5.4. Independent Element Results

A sweep test is shown in Figure 31 recorded in the time domain. Even at the lower frequencies tested, the printed hydrophone demonstrates a larger amplitude response.

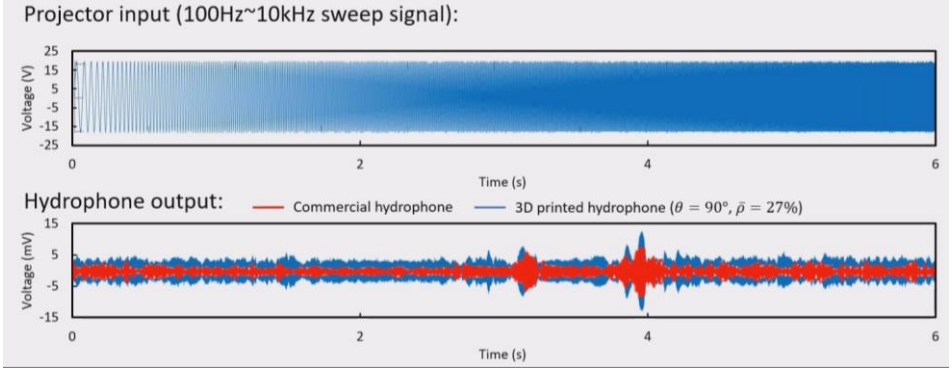

Figure 31. Amplified signal sweep in time domain: (top) input constant amplitude via signal generator to speaker, and (bottom) Commercial and latticed Hydrophone response across sweep

A larger manual sweep signal response revealed the relatively constant output of hydrophone working response leading up to resonance. In Figure 32, a series of tested points from the high-density foam lattice (HF) were plotted across a 1kHz to 60kHz range, demonstrating the heightened performance of the experimental hydrophone relative to that of the standard hydrophone.

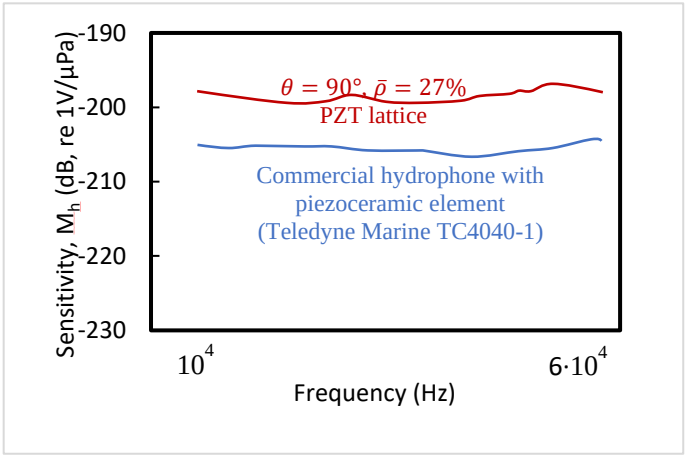

Figure 32. Frequency domain of calculated sensitivity: Comparison between Standard Commercial Hydrophone and the PZT Lattice

The Results of all lattice tests are plotted together in a bar chart up to their demonstrated resonance and sensitivity in Figure 33. This plot is additionally overlaid with the referenced value of the Commercial hydrophone and an estimated upper limit of the printable lattice frequency. Only 4 lattices are shown here due to damages in the assembly as expressed in the discussion.

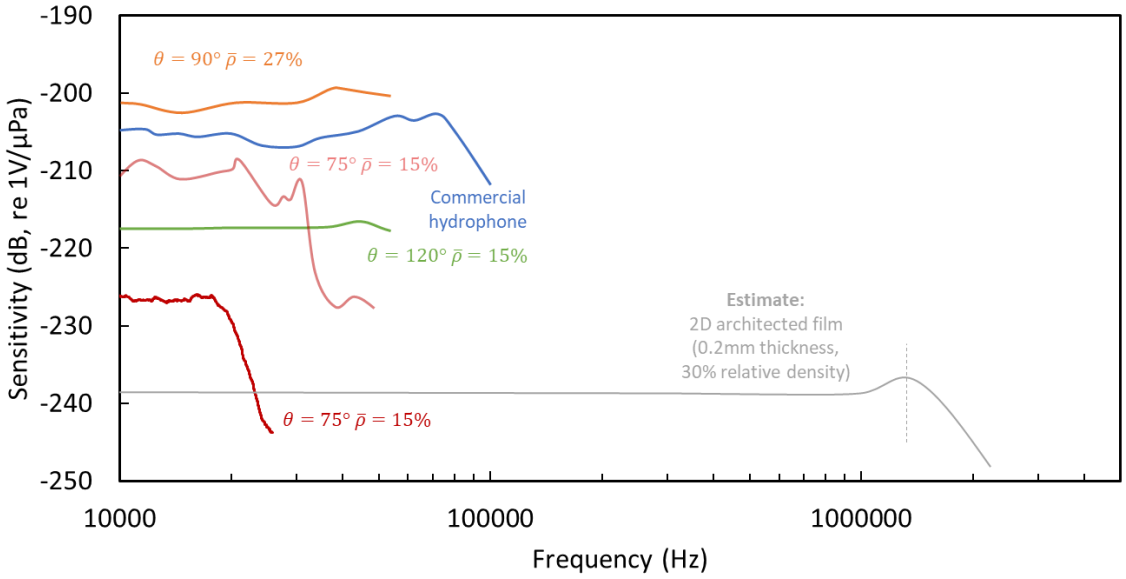

Figure 33. Results of the latticed hydrophone sweeps. The only high-density sample to perform without damage to the assembly is the high-density foam sample. This yielded the highest sensitivity as well due to a dominant sensitivity influence from relative density.

The working range agrees with the range expected from the latticing capabilities discussed in chapter 2, and the dense honeycomb lattice demonstrates a sensitivity greater than other elements measured.

5.5. Independent Element Discussion

The results were analyzed in context to the predicted values from Chapter 2. Further considerations for the data with regard to its being damaged are considered separate from reasons for variation from the predicted values, and the limitation imposed by COVID-19 are discussed.

The physical testing and remanufacture of some elements were unfortunately cut short as discussed in this section.

5.5.1. Meaning of Results

When comparing the results from testing to the theoretically predicted values, it was expected that impurities in manufacturing would yield reduced sensitivity across the board. The resulting values from the low relative density samples demonstrated this behavior. Whereas the expected sensitivities of the 15% relative density samples were -198dB and -187dB for LA and LH respectively, the data tests produced significantly lower results. This drop of approximately 15 dB is allocated to the error in production method causing reflections and suboptimal g_h values. This same error is believed to be the reason for the switching in behavior between the auxetic and foam structures, since it was expected that the auxetic structure would produce the weakest signal. The LF sample has suffered these handling damages to a degree that the operation of the element was at the noise level, preventing usable data from being obtained. On the upside, the increase in d_{33} and stiffness from the micro-architected design produced an expected increase in sensitivity and resonance behaviors, increasing performance with screw angle between the LA and LH samples shown.

The only functional high-density sample, unlike the low-density samples, performed at the expected sensitivity level. The increased impedance of the composite element was expected to produce greater reflections and worse performance than the low-density samples. A potential explanation for the high-density sample's improved performance is the unaccounted-for interaction effects on d constant from changes in relative density.

An additional consideration is that, at higher frequencies such as those being tested, the gaps between struts become too large for the structure to act as a single composite material. The small wavelength may influence echoes within the structure, confounding the data.

5.5.2. Data Considerations

While the data successfully captured shows promise in its analysis, there were multiple points which presented potential for error in the element performance or measurement system. Some prominent aspects are discussed briefly.

It was observed in the initial small tank trials that, despite the setscrew maintaining a hold on the cable, the element itself would not fully rotate. In this case, wire within the rubber sheathing was shifting. The shifting lead to breaking of the brittle electrode connections and cracks in the watertight seals. This rendered attempted test samples useless. In addition to electrical connection problems, the resonance modes of the small tank discussed in section 5.2.2. concentrated pressure at specific points in the small tank. This rendered directionality useless and made readouts appear randomized.

Moving to the Large tank, these problems were minimized, however damage to the brittle electrodes, while reduced, may have still been present, introducing error into the measurements. Inconsistencies in the waterproof coating of the hydrophone elements and the water-permeability of the selected coax cables may have influence variance in all response parameters slightly and sensitivity over time, respectively.

5.5.3. COVID-19 limitations

Despite great progress with respect to the manufacture and testing of transducers, the onset of COVID-19 had imposed limitations on the extent of testing to be carried out. Some uncertainty

within the data could not be retested to the extent of interest, and extended projects were made to be placed on hold indefinitely.

Complications of lab access from COVID-19 prevented the finalization of design and testing for the HIFU transducer, so the application of the transducer design framework to the printed curved elements is the extent of the contributions within this space.

Nevertheless, progress was made in manufacture and testing of additively manufactured acoustic elements.

Chapter 6: Integrated Lattice Testing

With the independent verification of tunable hydrophone characteristics of frequency and sensitivity, we may move forward to consider the tunability of directivity pattern, or beampattern, through integrated lattices, meaning multiple screw angles in a single element. While there are expected to be interaction effects on frequency, the tuning of beampattern at a single frequency is tested. This chapter is decomposed into the specific scope of beampattern control, the manufacturing of integrated lattices, modifications to setup, methods, results, and discussion.

6.1. Directivity Pattern Control

Elements were designed with multiple selected lattice screw angles adjacent to each other, such that the response of the beampattern, is tuned. These PZT elements were manufactured to demonstrate the control of beampattern in the XY plane at a constant frequency.

Ideally, this is applied to a cylindrical element-or even spherical to ensure constant distance from the source during rotation. These tests, however, were not carried out within the time frame prior to onset of COVID-19, so tests shall be omitted from this work.

6.2. Multi-lattice (Integrated) Element Manufacturing

Combining various lattices, the lattice elements were printed using the same system in section 4.1. In the event of excess wear on the PDMS film from too many print layers, the prints could be segmented into two separate prints to be adhered together via PEGDA during post processing. The sintering step would enable removal of the additional PEGDA while the PZT undergoes densification, combining the lattices.

2 lattice combinations were selected to demonstrate the tunability of beampattern due to differing screw angle and relative density. The Low-density Honeycomb (LH) lattice and High-density foam (HF) lattice were selected for their representativeness of the designable range of

frequency and responsiveness. These lattice elements are seen as separate elements in the 0. The two combined elements formed a rectangular prism formed from 4 lattice elements oriented in a square. The selected screw combinations are observed in the results such that two adjacent HF lattice elements are combined with 2 adjacent LH elements. This was compared to an element consisting of 2 HF and 2 LH lattice cubes (Figure 34) matching only on the diagonals.

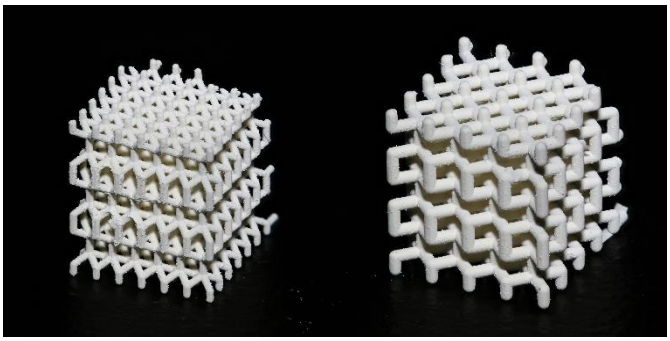

Figure 34. (Left) low density honeycomb, 120 degrees (Right)high density foam, 90 degrees

Updating casing design—The casing was updated according to the case design workflow established above. The resulting cases fit each element as intended, and electrodes were applied to the top and bottom of the elements during assembly, ensuring electrode contact with all lattice element subcomponents.

6.3. Setup for Integrated Element Testing

While the setup for the 2D beampattern samples used the same electrical systems and the mechanical rigging for the speaker, the testing of a 2D beampattern demanded modifications. Fixture design was necessary to enable a minimum of 8 angular datapoints.

An initial design of an angle-controlling mount for the small tank was developed, granting 8 measurement positions. The fixturing used a setscrew to hold the hydrophone tightly in-place as the hydrophone was rotated 45 degrees at a time. A closely tolerance cylinder with 8 set points

ensured accurate angle changes. Issues presented themselves as expressed in the discussion section below, and the final fixture was developed for the large tank.

In the large tank, A PVC dial seen in Figure 35 was built, identifying 22.5. degree intervals about the joint to enable 16 test points. The wiring was adhered to the rotating vertical PVC pipe to prevent wire-kinking, and wire was gently handled to prevent any damage to electrodes.

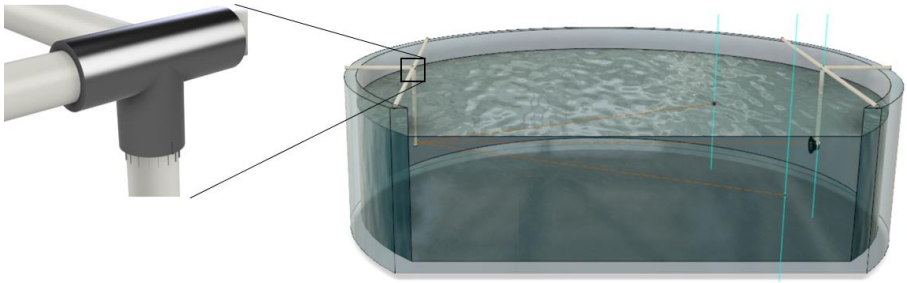

Figure 35. PVC fixture dial for large-tank directivity measurement at 22.5-degree divisions. Markings are aligned between the T-joint and the vertical PVC mounting piece to achieve controlled angle steps of a fixed amount.

The 15-degree offsets for speaker placement on either side of the of the of the centerline enabled the twisting of wires on rotation was not interfering with the signal. Though, it was noted that the resonant pressure field produced by a circular tank may amplify differences observed, so this “sanity check” was not used for quantitative data collection.

6.4. Integrated Element Test Methods

To test the tuned beampattern of the combined lattice elements, each of the two lattices elements is measured at a constant distance of 3.5 meters from the speaker held at 7KHz. 16 measurements are taken per combined element, one at each angular position set on the PVC fixture dial. The response at 7KHz signal, read out through an FFT function of the oscilloscope, was manually recorded with the angular position. The resulting signals were normalized using equation 1.8 and plotted on a polar coordinate system. The expected response is calculated based on the

selected elements being used, applying their sensitivities, and the prediction is scaled to match the outer bound of test results, thus eliminating any error in constant inefficiencies between the experiment and prediction.

The calculated and normalized beampattern is then compared to a predicted response. The prediction considers the sensitivity of each element and maps it, to 16 points, wherein each element is responsible for 3-4 angular intervals. A smooth line connects the points for ease of visual interpretation. Further limitations of this representation are discussed in section 4.3.3.

6.5. Tuned Directivity Pattern Results

The resulting elements and respective directivity pattern shows are shown in Figure 36, normalized from 0 to 1 to observe the change in sensitivity with respect to element orientation.

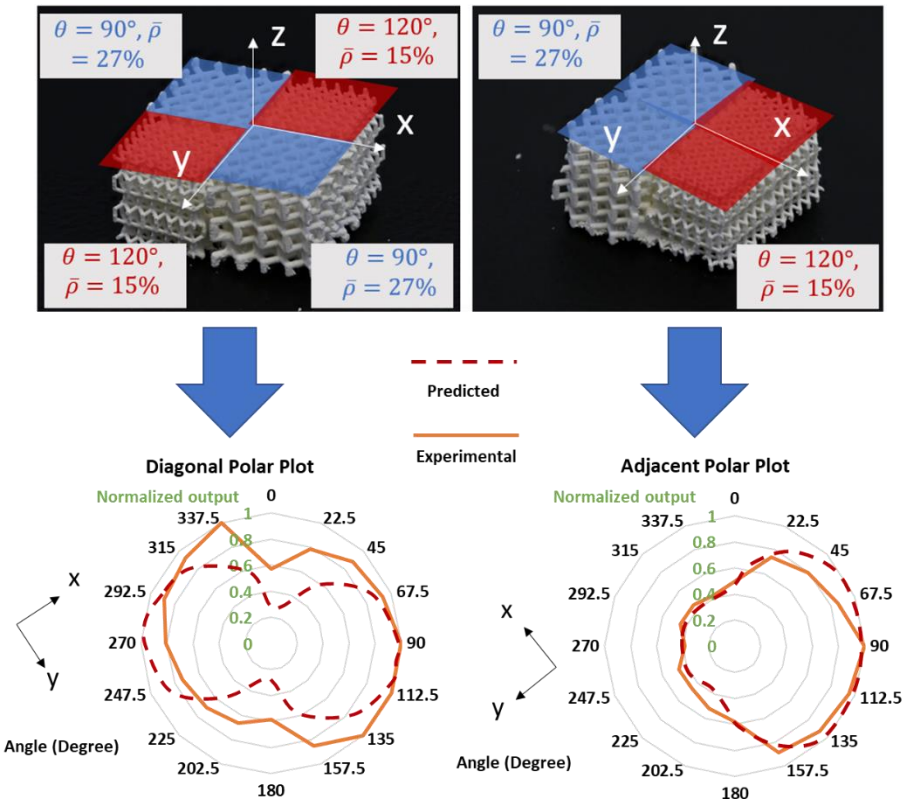

Figure 36. Integrated elements for tuned directivity pattern and their respective testing results vs expected results: (Left) Diagonally matched lattice element design for low-density honeycomb, LH, and high-density foam, HF; (Right) Adjacently matched lattice element design for LH, HF.

6.6. Discussion

The responses of the combined lattice elements closely resemble the expected results of the test, validating our hypothesis for tunability and design of an acoustic directivity pattern via micro-architected lattice elements. The results presented in Figure 36 additionally align with the unexpected relative density relationship observed in Figure 33 wherein the higher relative density resulted in a higher sensitivity, since the HF lattice has a normalized value of 1, greater than the LH lattice.

The slight variance from the predicted results additionally appears to be systematically skewed, meaning that the data is more partial to one direction, losing sensitivity on the mirrored side. This may be a result of the transducer being angled one direction while the waterproofing sealant dried. Since the sealant may drip, a tilt while drying may weight 1 side of the hydrophone with more signal attenuation than the other. This would yield a directional skewing of the directivity pattern. Alternatively, if the wire itself contained a slight bend, the element itself may have been shifted marginally towards and away from the speaker as it rotated. Small variation such as this are even visible with existing commercial hydrophones.

Major sources of error in the measurement stemmed from wire handling, despite efforts to keep this type of error to a minimum.

To minimize bending in the wire, the wire was maintained in front of the PVC cross-section; this required starting with the wire slightly bent ~180 degrees from the back in the initial and final positions of testing. The 180-degree mark enabled a completely straight wire.

The wire handling and the water-permeability of the low-cost coax cables gradually accumulated noise in the signal over the course of testing. This limited the repeatability for a single element's testing; however, the retest of an initial position would produce only a small reduction of ~1% of the signal. The change in sensitivity relative to angular position exceeded this, affirming

that this did not confound the validation of results. This signal error over time may be the source of the gradual reduction of signals around a constant lattice type, wherein the expected beampattern is constant.

Other reason for the tested result's variance from the expected result is based in the current manufacturing method. The method of manufacture combines 4 independently printed elements sealed together in postprocessing. The combined element on the left can be seen to house a defect at the joining between the two lattices. This results from the variations between samples of the same type and the meshing of lattices of different types. For early stages of prototyping and proof of concept, this error was acceptable. In a similar vein, these lattices are not continuous at a lattice-changing interface, so the produced beampattern should not be expected to be continuous. For simplicity, the portrayal of the beampattern efficiently communicates the concept, however, and the discontinuity at the interfaces can be observed such as that shown in the testing result of the right lattice at 123.75 degrees. Lastly, the geometry of the assembled cubes confounds with the ideal expected beampattern. Ideally all outer faces of the lattice will be equidistant from the center point in a form such as a cylinder.

Future work unexpressed here has already taken steps to manufacture and test a cylindrical lattice element for precisely this reason.

Chapter 7: Product Framing for Industry

After confirming the fundamental functions of the technological hypothesis, a product was generated, pushing the technology to perspective potentials. The theoretical product is rendered to communicate the product concept and bring it to reality as to reachable potential, and a workflow is developed to enable a high-speed design generation and ease of tuning for an even more industry-ready system.

7.1. Geometric Design for Multi-planar Beampattern Design

Beampattern design is demonstrated across the X-Y plane in this work, however the application of this technology does not stop in a single plane. Future work enables the application of this tunable within all 3-dimensional space with respect to both a polar angle and an azimuthal angle in a spherical coordinate system. This tunability is theorized through the tuning of lattice structures within a sphere by modifying the localized microarchitecture and thickness.

This extended work is initially explored through the generation of a spherical lattice element which is designed via Autodesk inventor, parameterizing the design of a unit cell with respect to radius of the sphere, the length of the center strut of a unit cell, the strut angle, and the strut thickness. Similar to 0, but curved based on the defined radius, the lattice unit cell was rotated about both the x axis to form a ring and the z axis to generate a sphere. Interlinking nodes needed to be generated to ensure the complete geometry. These nodes were parameterized based on radius and strut length as well.

Segments of various lattice structures were paired together to achieve a tuned beampattern wherein the center band of the sphere is more responsive than its top and bottom components. This lattice had the casing workflow applied to it and was brought into Fusion 360 for figure generation.

7.2. Realistic Rendering

A workflow was developed to bring in the inventor-generated lattices to Fusion 360 for rendering of the design. Figure 37 shows the rendered output from Fusion 360 after design practices are exercised.

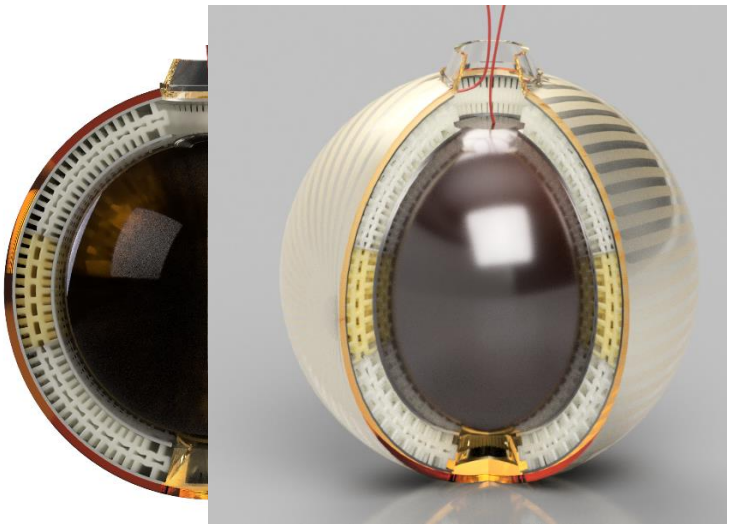

Figure 37. Realistic render of tuned lattice element for designed beampattern in all axes. The left render reveals the variability between lattice structures

By rapidly visualizing the produced element as a realistic rendering, stakeholders of the project can more easily come to an understanding of expected outcomes, can grasp the concepts, and assist in financially pushing a project forward. Members of a team will benefit from a realistic portrayal of a product through an instant understanding of expectations for manufacture intent. This early-on detailed communication will surface potential design flaws earlier and garner motivation within the team to bring the prototype to reality.

7.3. Enabled Mass-customization via Field-Driven Design

To make the design process feasible for industrial use and to enable the true freedom of design, rapid design changes and selective spatial tuning of lattice type and lattice thickness must be continuous. The use of “Field-driven Design,” as used in the nTopology software enables such

design freedom [86]. Additionally, the recent contributions of Liu offer insight into potential future options for merging lattice types in a continuous manner.

To enable user design of such a space, a Microsoft Excel file was generated to take in polar coordinates and associated amplitudes (resembling an intended sensitivity value). The file converts the user inputs into a cartesian point cloud which is imported into the nTopology software. An automated modular workflow was developed within nTopology to take in the input, generate a continuous field from the user data, and output a lattice with variable thickness in accordance with the designed sensitivity field. In a similar way, a field can additionally be generated similar to the output of a stress analysis for automated transducer design for a specifically designed use case. An example field and its associated lattice formation are shown in Figure 38.

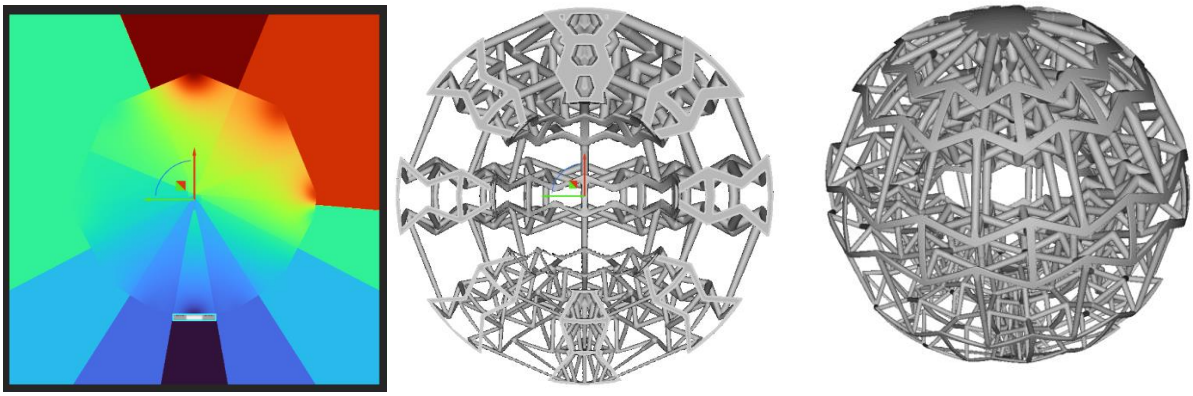

Figure 38. (left) planer slice of user-input sensitivity requirements. (middle) cross section of Auxetic lattice with strut-thickness tuned according to the user-input sensitivity field. (Right) Full lattice tailored to specific needs of the user.

The development of such a workflow, combined with the technological advances presented within this paper open the gates for very low-cost, low power, compact monitoring systems as well as acoustic detection specifically designed for minimal noise specific to a selected space.

Chapter 8: Customer and Value Chain Discovery

An advancement in technology is beneficial for advancing science, but to initiate widespread change in the world around us, we must take the technology a step further to discover the scope of customers and value chain who care about and benefit from such a technology. More than this, we must seek to realize if the benefit provided will be valued by the perceived users by filling a need they have. It is reasonable to research a fascinating technical problem for curiosity and interest, however as scientists and engineers we should seek to develop the science around problems that matter. By establishing this link to industry, advancing the early technology readiness level (TRL) of critical science, and demonstrating its importance to society, authors will enhance their impact and recognition, gaining recognition as a leader in their field while making a greater impact on society.

8.1. Methods Considered

Steve Blank expresses the Lean Launchpad methodology through the NSF I-Corps program curriculum and process as a means to discover customer segments who can not only benefit, but who have a present need for the capabilities enabled by the newly developed technology [4]. Dr. Alejandro Salado expresses the systems approach for eliciting customer needs and defining a problem space through which a solution space can be mapped [87]. Tools from both the Lean Launchpad method and Salado 2021 are used to seek out, identify and clarify a problem space fitting of this solution.

8.2. Approach and Initial Hypotheses

In this chapter, I present the customer discovery process through a lens of “technology push” in search of a “market pull” to validate the value of the newly developed technology as a means to directly address the problems faced by customers all throughout the value chain. I take the final

step to bridge technology from a novel research concept to a profitable business opportunity. In this way, I am mapping a series of hypothesized solution spaces and testing for the presence of a matching problem space in and around each solution space.

The push-validation process is iterative, wherein the exploration of an initially hypothesized solution space leads to not only the validation or rejection of the hypothesis but also the discovery of a newly emergent hypotheses. The search for evidence-based validation (or rejection) from customers and the value chain in both the original and the new hypothesized spaces continues until there is sufficient support to confirm or reject the hypothesis. The amount of support needed to feel confident will vary with the risk tolerance of an individual along with other confounding factors. The ways in which questions are asked will influence bias, drawing out validation or influencing rejection. Overconfidence and attachment to an idea may also drive bias within the one who is testing the spaces. The objective is to eliminate as much bias as possible to understand the true pains, gains, and perceptions of a potential user [5].

The process is broken down here into 2 stages: initial hypothesis generation and problem space validation/identification. As discussed, the process is iterative, so the findings of problem spaces will exceed the initial hypotheses generated for the spaces. Both the initial and new problem spaces are consolidated into stage 2 of this work. A list of questions asked to prompt responses that identify and validate a matching problem space are included in appendix B. 17 interviews were conducted to date, and all names/organizations are anonymized to the associated or neighboring markets to which they operate in.

To draw a mechanical parallel to the situation, imagine a plane with varying point masses scattered about. Each mass represents a group of customers (the “customer mass”) which is correlated to how much how many customers exist and how badly they want a solution. Each

customer mass has an associated gravitational pull (the "customer pull") which expresses this need; the more customers there are and the more they want a solution the more the customers will pull one who moves into the space towards a solution. From an initial point on the plane, we launch into three point-clouds (our 3 industries) in search of the greatest customer pull while getting pull from many directions. I call this representation the "Mapping gravity of the problem," since this plane on which the problems exist enables the mapping of various problems and the gravity of that problem. A generalized depiction of this representation can be observed in Figure 39.

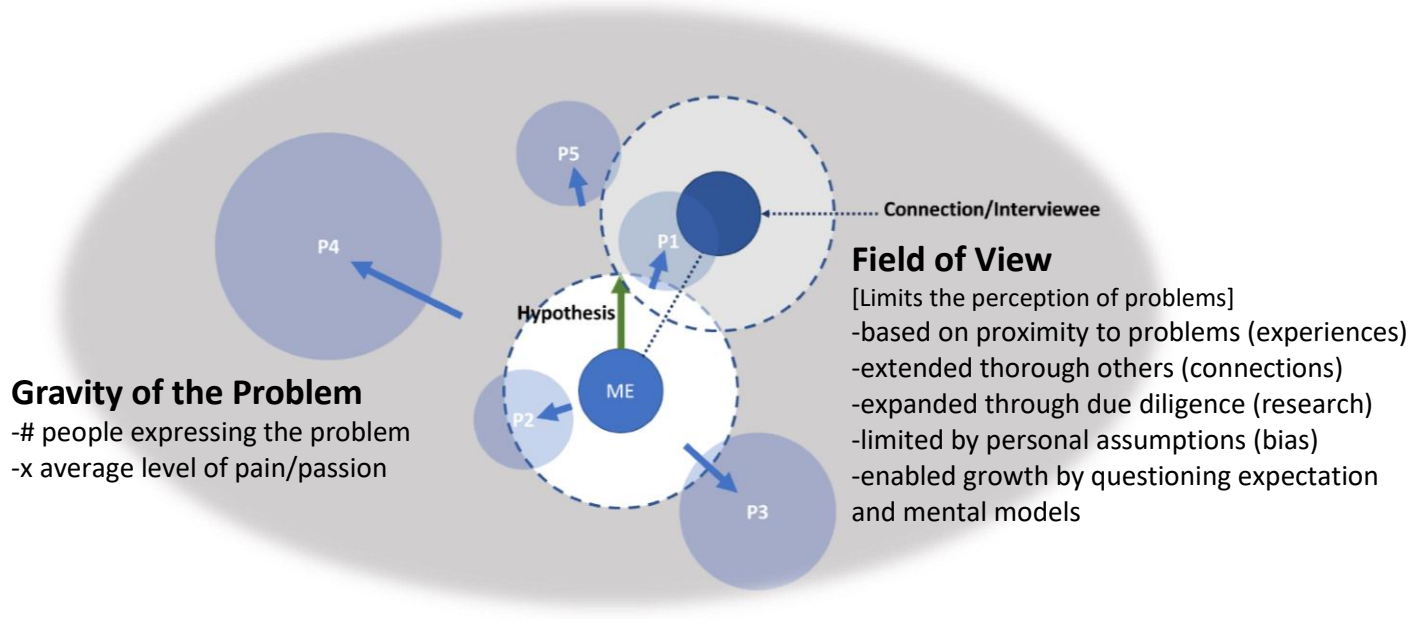

Figure 39. Identifying and Mapping Gravity of the Problem (Space). The representation of the gravity of the problem and the process means through which it can be mapped shows that you start with an initial field of view through which you are aware of existing problems (some you are more aware of than others). Some problems, such as P4, are completely unknown, yet hold great potential. Problems such as P5 may be discovered through the expressions of a connection or an interview. This may influence a hypothesis to investigate the problem. Depending on where you set your course (hypothesis) through the space, you may encounter problems along the way and be pulled in different directions. If you are willing to question your expectations/mental models as expressed by Peter Senge, you will be open to feel the pull of the customer's needs, which may lead to discovery of something even greater.

8.3. Initial Hypotheses

Initial hypotheses were developed in three industries. The first of the industries works in close collaboration with the lab (Underwater Naval applications), and the other two industries are rapidly

growing, with perceived applicability for the presented technology (medical devices and automation).

8.3.1. Underwater Hypotheses

Underwater acoustics at the ultrasonic range was hypothesized to assist ships, submarines and testing systems, providing clearer signals from reduced noise reflected into the sensing element. The tuned beampattern could produce an element designed for the vehicle or testing facility to achieve the intended result. SONAR (specifically passive) and communications were additional areas of interest in the space wherein the signal to noise ratio (SNR) could be improved, and specific frequencies could be selected to be heard. These applications were expected in both the public and private sectors.

The hypotheses we propose here are: Sonar SNR is currently a major concern for the US Navy. Underwater testing facilities will become more effective with customized directivity patterns made to the space.

8.3.2. Medical Hypotheses

Medical device applications were hypothesized to benefit from the complex element forms that could be created to fit in hard-to reach locations and to generate greater pressures in HIFU applications. It is believed that such higher pressures could enable faster wireless charging of implants and extend the limits of current methods of pressure treatments. In the diagnostic space, the tunable beampattern is hypothesized to enable catheters and echo-ultrasound systems to have improved signal amplitude by blocking out noise from specific parts of the sensing device.

The hypotheses here are: Implants and treatments seek to achieve higher acoustic pressures outputs? SNR is major concern for the Ultrasound imaging.

8.3.3. Automation Hypotheses

In the spaces of automation, hypotheses were developed initially around autonomous driving vehicles. It was believed that problems exist in the use of ultrasonic sensors to obtain clear data. Thus the use of beampattern tuning could improve automation through clearer data collection. This would reduce the amount of processing time and thus power which must be applied to enable automation. Through interviews, this hypothesis, was extended into the industrial automation sector where robotics and collaborative robotic arms are becoming increasingly prevalent.

Hypotheses in this space are: Ultrasonic sensors used in automobiles/robotics demand greater signal to noise ratio. Designers of autonomous systems need reduced processing time and reduced power consumption from sensors.

8.4. Identified Problem Spaces

After establishing hypotheses, interviews were conducted with those who could affirm or reject the hypotheses. The problem spaces they express are consolidated into the three initial areas: underwater problem spaces, medical problem spaces, and automation problem spaces. Extensions adjacent to the spaces are included within, and all interviews consider the context that the tuning of directivity pattern in this way will not directly solve the problem. It is simply a step in the direction of achieving a solution to the identified problems within the problem space.

8.4.1. Underwater Problem Spaces

Multiple Naval interviews and online sources validated the hypothesis that SNR is a major concern [55], [64], [67]. This was particularly found to be the case in the application of sonobuoy, devices dropped into the ocean to identify and track submarines, marine life, ocean contours, etc. based on the changing needs of a given sonobuoy, there must be multiple elements with various directivity patterns at once on one of these single-use devices. The customization of elements in

the ways presented in this paper may enable the consolidation of such element needs. In addition to sonobuoy, there are towed and conformal arrays for passive sonar systems on ships and submarines. During operation, these vessels emit large acoustic signatures from onboard systems, propulsion systems, etc. These confounding signals demand that the towed array of sonar elements is towed hundreds of yards from the back of the ship. According to Jon Greene, having served decades in the navy, blocking this direction of sound response offers a much-needed improvement in SNR, and any improvement on this front is valuable. In these conversations, it also emerged that the frequencies utilized in these spaces are often sub-ultrasonic. This is valuable to note, as there is still tunability into this range, and this leads into an additional concern around attaining all frequency ranges (you never know what frequency the enemy will be operating at) (J. Greene, personal communication, April 7, 2021).

Going against the expectation of the original hypothesis for a considered problem, it was realized that underwater testing facilities are not of too much concern. Whereas this transducer was expected to impact test facilities, interest was always averted to on-board applications.

Other problems were additionally expressed offering new problems to investigate. While still untested, these are: achievement of more direct communication through more precise signal emission and (less concerned) signal reception. It was expressed that the nonlinear pathways of in-ocean propagation make knowing the direction of a signal difficult, and there was even talk of autonomous underwater systems which can certainly benefit from the improved SNR discussed above. Lastly, the on-board monitoring for cracks upon submersion and maintenance monitoring via acoustics was brought up around the incredibly important need to know that a submersible system will not fail at high pressures such as those experienced by submarines. While not tested, these show even greater unexplored value from the technology.

Within this space overall, the SNR is deemed as a major priority, the hypothesis for facility needs is rejected, and new opportunities for hypotheses have emerged for the future.

8.4.2. Medical Problem Spaces

Conversations on medical devices were difficult to come by, based on the busy schedules of doctors in this pandemic season. This brought about a significant space of catheter application in detecting pneumonia; there is a need to navigate, visualize, and in some cases interact. A single element for sonar in this case only gives a single point of information, but through the work presented here there may be an opportunity to provide greater insight from a similarly sized element. On this front, improvements in interaction (potentially through acoustic pressures), navigation and visualization could be achieved through improved SNR. While this seemed promising, an interview with Dr. Eli Vlaisavljevich revealed that needs of catheters in the space of sonar are not in SNR, but moreso in size consolidation of arrays (E. Vlaisavljevich, personal communication, April 27, 2021). Since it is still unclear as to the extent of meaning which can be garnered from a single tuned element in a catheter, this interview influenced a rejected outlook on the first of the medical hypotheses.

While no interviews could take place with wireless implants, there were interviews around the difficulties of implants in general, leading to the rejection of the hypothesis that higher pressure would be beneficial. This rejection is based on the regulations of pressure by the FDA emitted into the body. The main points of concern in this space are based in the doctor's code for "do no harm". According to a doctor from UCLA Health, all efforts should be made to reduce the invasiveness of a procedure, and while this is promising for the creation of complex geometries to enable minimally invasive devices, this does not validate our hypothesis of a need for improved SNR (no

direct uses were discovered in this space outside of the Sonocloud^{TM} technology) (UCLA Health Doctor, personal communication, March 3, 2021).

Other areas expressed are the need for higher frequencies for better resolution in small animal research uses of ultrasound imaging. For ultrasound imaging, there is satisfaction around the current solutions for gel used in echocardiograms or other external imaging systems, and there was a significant irritation around the need to hold your hand very still when imaging small parts of living beings. While there may be solutions for these problems, the high cost of systems outside the ballpark of $100k were not perceived valuable enough to be purchased.

One final significant issue that existed in the extraneous spaces was the ability to monitor moving animals, such as rats. Currently, almost all research is conducted in the space of animal studies on drugged rats for ultrasonic imaging. A conformal solution to stay on the rat while uninhibited could yield great impacts in the field of live animal studies (Animal Ultrasound Doctor, personal communication, March 23, 2021).

Within this space overall, the SNR does not appear to create a significant enough need from medical device users, and higher pressure for acoustic implants is not desired. These findings reject both initial hypotheses in the medical device problem space, however there may be potential in other discussed problems to have surfaced along the way.

8.4.3. Automation Problem Spaces

The final problem space uncovered addresses the selection of sensors in robots and autonomous vehicles. While there are sufficient sensors currently used for distance sensing in vehicles, the single point that is yielded by an ultrasonic echo is not believed to be valuable enough to be integrated into an autonomous system more fully. This applies to both vehicles and robots; in robots a simple laser can measure the same result with greater reliability and a similar cost. This

brings up the decision factors of a sensor being selected by a system designer: ease of access (which we cannot do anything about), reliability, and performance. With this, our hypothesis for improved SNR benefiting robotic/driverless systems is partially confirmed (Collaborative Robotics Designer, personal communication, March 23, 2021). Since the interviewed individuals did not currently use sonar systems because of excess noise, this reveals a clear need in the sonar space. The combination of directivity pattern control in arrays may overcome the other shortcomings of current sonar sensors.

While the concern for power being used was never expressed, nor a need for data processing reductions, there was talk of the large data output from cameras that can be difficult to handle. Nevertheless, this hypothesis is rejected (D. Conte, robotics researcher, personal communication, April 35, 2021).

One additional problem which became prominent enough to be considered and tested as a new hypothesis is the following: designers of automated systems seek out low-cost sensing redundancy. LIDAR sensors (used in both the automotive and robotics spaces) are very expensive but have blind spots. In autonomous vehicles, some methods to fill these spots still cost in the ballpark of $10k. Providing a low-cost solution to identify if an object has entered the blind spot could provide autonomous vehicles with significant cost reductions. These concepts open up the conversation around gaps or redundancies in any security system-not just robots and cars (Autonomous Vehicle PM, personal communication, March 15, 2021). Compounding this need with the customization presented within this work, the precise region of need can be monitored by a designed element as seen in Figure 40, even avoiding ground reflections.

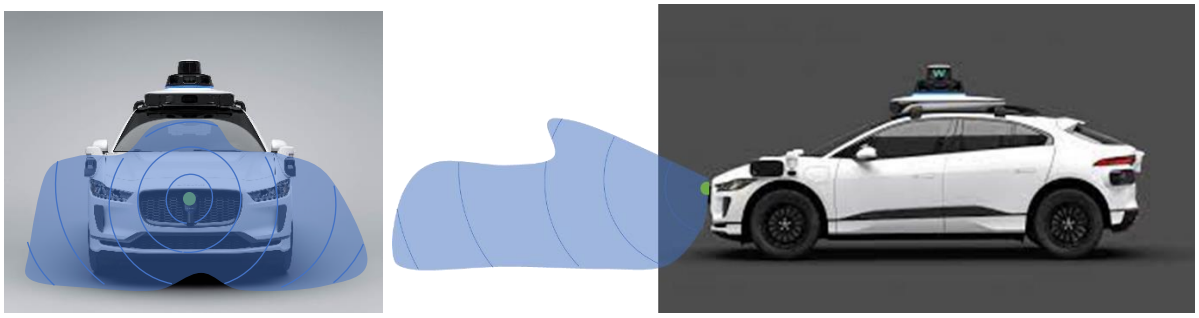

Figure 40. Customized directivity pattern, possible through the presented work, covers front blind spots on a Waymo autonomous vehicle [81].

Within this space overall, the SNR has a clear need for improvement of sonar in automated systems, validating our first hypothesis. Our second hypothesis: the need from designers for reduced signal processing and power consumption through reduced data transfer in automated systems was rejected. In addition to the two initial hypotheses, a third hypothesis was additionally created and validated that low-cost redundancy is needed in autonomous system design.

8.5. Confidence in Findings

Upon completion of 20+ interviews, there were many discovered problem spaces, but only a limited few expressed explicit interest in a way where the technological advancement was a genuine need for an existing problem. For the spaces of robotics, automotive, and entertainment, there is significant need for greater technology advancement. In the medical spaces, catheters appear to be the closest device in-need of the tunable beampattern, however even they are satisfied with current existing solutions. This is even moreso the case for ultrasound devices—though the size of market for echocardiogram advancements is large. The space of naval applications, as it relates to the voiding of significant acoustic noise emitted from a ship in the application of towed hydrophone arrays, is a great need. The technology for directivity pattern control is an ideal fit for the job along-side that of sonobuoy. Rob Bishop, a knowledgeable operator of the naval weapon systems stated, “If we can affect our directivity index, it will further enhance our ability to increase

that probability [of keeping the country safe].” Nevertheless, there were only 4 interviews discussing this topic, so at least 1more interview with stakeholder(s) from another organization will enable a great enough confidence to move forward, enabling a broader use of the technology in a public space.

An additional consideration to dive deeper is the late-considered security systems for sonar (not underwater). While this may only work for small spaces due to signal attenuation, the conversation of robotic security/safety systems revealed the high-cost solutions that currently exist in these spaces. This space shows potential as a new innovative technological solution which currently non-existent in markets. The customer validation will need to be very significant before diving deeper into such a space, but this discovery process would be well-spent exploring.

Chapter 9: Conclusion

9.1. Conclusion

In conclusion, the concept for a tunable ultrasound sensor was taken from a concept to a technology directly beneficial to a multitude of commercial spaces. The hydrophone sensitivity, resonance and beampattern were predicted through models from chapter 2 and tested in chapters 5 and 6. While the results varied from the expected response, trends of tunability were observed in the data, showing promise in the concept. A framework for transducer manufacturing was developed and carried out through chapters 3 and 4, including the contribution of a mathematical model for printability in a bottom-up MIP-SL system. The model effectively considers exposure time and layer count as it relates to PDMS wear in the calculating the suction force on a part throughout the printing process. In chapter 7, the technology was considered in a context of commercialization by developing a rendered spherical transducer and rapid workflow for customization of a lattice in a continuous workspace, as opposed to the discrete lattice combinations tested in chapter 6. Finally, a method of technology push was set up by adapting the NSF lean launchpad approach. Through a series of hypotheses and tests, the naval application of towed arrays shows the greatest promise for the technology as a commercial application.

The significance of these results is grounded in laying a foundation for future success. The contributions on the front of the tuned hydrophone beam pattern lay a groundwork for successful tests soon. The development of methods in the space of the transducer and continuous element tuning accelerates prototyping into the future and open opportunities for more funding, allowing for further developing the technology. The resulting identified problem spaces enable the greatest impact to be made once the technology reaches an appropriate readiness level. This impact spans

national security, local security, improved diagnosis of disease, lower cost solutions for autonomation solutions, and more.

9.2. Future Work

Moving forward with the foundation set for accelerated success, the most immediate action to take is to remanufacture and retest the samples. Minor modifications may be made to assist in the encountered issues of brittle electrode connections and poor waterproofing of the wiring. The spherical lattice element and continuously tuned lattice element are to be printed and tested, using the methods within this thesis, and once at a functional point, steps may be taken to partner with and enable solutions for those who were identified to benefit from the technology. Additionally, since the only spaces considered here were high-frequency, investigation of low-frequency scaling for the technology should be investigated as well. There may be opportunities to improve the world waiting below the places you least expect (that is below the frequencies we addressed within this paper.)

References

[1] I. R. Sinclair, “Sensors and Transducers (3rd Edition),” pp. 1–9.

[2] R. Wang, S. Liu, C. R. Liu, and W. Wu, “Data-driven learning of process−property−performance relation in laser-induced aqueous manufacturing and integration of ZnO piezoelectric nanogenerator for self-powered nanosensors,” *Nano Energy*, vol. 83, p. 105820, May 2021, doi: 10.1016/j.nanoen.2021.105820.

[3] B. Long, S. A. Seah, T. Carter, and S. Subramanian, “Rendering volumetric haptic shapes in mid-air using ultrasound,” *ACM Trans. Graph.*, vol. 33, no. 6, pp. 1–10, Nov. 2014, doi: 10.1145/2661229.2661257.

[4] S. G. Blank and B. Dorf, *The startup owner’s manual: the step-by-step guide for building a great company*. Pescadero, Calif.: K & S Ranch, 2012.

[5] A. Osterwalder, Y. Pigneur, and T. Clark, *Business model generation: a handbook for visionaries, game changers, and challengers*. Hoboken, NJ: Wiley, 2010.

[6] J. L. Butler and C. H. Sherman, *Transducers and Arrays for Underwater Sound*. Cham: Springer International Publishing, 2016.

[7] W. W. L. Au and M. C. Hastings, *Principles of Marine Bioacoustics*. New York, NY: Springer US, 2008.

[8] V. Sharapov, Z. Sotula, and L. Kunickaya, *Piezo-Electric Electro-Acoustic Transducers*. Cham: Springer International Publishing, 2014.

[9] A. Wei, “Design, Analysis, and Application of Architected Ferroelectric Lattice Materials.” Virginia Tech Department of Mechnanical Engineering, May 03, 2019.

[10] M. de Jong, W. Chen, H. Geerlings, M. Asta, and K. A. Persson, “A database to enable discovery and design of piezoelectric materials,” *Sci. Data*, vol. 2, no. 1, p. 150053, Dec. 2015, doi: 10.1038/sdata.2015.53.

[11] V. Yu. Topolov, P. Bisegna, and C. R. Bowen, *Piezo-Active Composites*, vol. 185. Berlin, Heidelberg: Springer Berlin Heidelberg, 2014.

[12] J. Curie and P. Curie, “Développement par compression de l’électricité polaire dans les cristaux hémièdres à faces inclinées [Development, via compression, of electric polarization in hemihedral crystals with inclined faces],” *Bull. Société Minéralogique Fr.*, vol. 3, no. 4, pp. 90–93, 1880, doi: 10.3406/bulmi.1880.1564.

[13] H. Kim, F. Torres, Y. Wu, D. Villagran, Y. Lin, and T.-L. Tseng, “Integrated 3D printing and corona poling process of PVDF piezoelectric films for pressure sensor application,” *Smart Mater. Struct.*, vol. 26, no. 8, p. 085027, Aug. 2017, doi: 10.1088/1361-665X/aa738e.

[14] F. Sun and D. Chen, “Ferroelectrics for Biomedical Applications,” p. 4.

[15] R. S. Dahiya and M. Valle, *Robotic Tactile Sensing*. Dordrecht: Springer Netherlands, 2013.

[16] H. Cui *et al.*, “Three-dimensional printing of piezoelectric materials with designed anisotropy and directional response,” *Nat. Mater.*, vol. 18, no. 3, pp. 234–241, Mar. 2019, doi: 10.1038/s41563-018-0268-1.

[17] J. Sirohi and I. Chopra, “Fundamental Understanding of Piezoelectric Strain Sensors,” *J. Intell. Mater. Syst. Struct.*, vol. 11, no. 4, pp. 246–257, Apr. 2000, doi: 10.1106/8BFB-GC8P-XQ47-YCQ0.

[18] B. Praveenkumar, H. H. Kumar, and D. K. Kharat, “Characterization and microstructure of porous lead zirconate titanate ceramics,” *Bull. Mater. Sci.*, vol. 28, no. 5, pp. 453–455, Aug. 2005, doi: 10.1007/BF02711235.

[19] R. W. C. Lewis, A. C. Dent, and C. R. Bowen, “Network Modelling of 3-3 Piezocomposite Materials,” *Ferroelectrics*, vol. 351, no. 1, pp. 216–224, Jun. 2007, doi: 10.1080/00150190701354307.

[20] H. Kara, R. Ramesh, R. Stevens, and C. R. Bowen, “Porous PZT ceramics for receiving transducers,” *IEEE Trans. Ultrason. Ferroelectr. Freq. Control*, vol. 50, no. 3, pp. 289–296, Mar. 2003, doi: 10.1109/TUFFC.2003.1193622.

[21] D. P. Skinner, R. E. Newnham, and L. E. Cross, “(Received April 20, 1978; Refereed),” vol. 13, no. 6, p. 9.

[22] M. F. Hackathorn, “The Design of a Deep Ocean Hydrophone,” p. 54.

[23] M. B. Moffett, J. M. Powers, and J. C. McGrath, “A ρc hydrophone,” *J. Acoust. Soc. Am.*, vol. 80, no. 2, pp. 375–381, 1986, doi: 10.1121/1.394088.

[24] F. Fahy and P. Gardonio, *Sound and structural vibration: radiation, transmission and response*, 2nd ed. Amsterdam ; Boston: Elsevier/Academic, 2007.

[25] J. V. Kinsler Lawrence E. ,. Frey, Austin R. ,. Coppens, Alan B. ,. Sanders, *Fundamentals of Acoustics*. John Wiley & Sons, 1999.

[26] I. D. Groves Jr, “The Design of Deep-Submergence Hydrophones.” Defense Technical Information Center, Sep. 03, 1971, [Online]. Available: https://apps.dtic.mil/sti/citations/AD0729643.

[27] A. Hurrell and P. Beard, “19 - Piezoelectric and fibre-optic hydrophones,” in *Ultrasonic Transducers*, K. Nakamura, Ed. Woodhead Publishing, 2012, pp. 619–676.

[28] B. M. Abraham, “Low-cost dipole hydrophone for use in towed arrays,” in *AIP Conference Proceedings*, Mystic, Connecticut (USA), 1996, vol. 368, pp. 189–201, doi: 10.1063/1.50338.

[29] I. Gibson, D. Rosen, and B. Stucker, *Additive Manufacturing Technologies*. New York, NY: Springer New York, 2015.

[30] X. Zheng *et al.*, “Design and optimization of a light-emitting diode projection micro-stereolithography three-dimensional manufacturing system,” *Rev. Sci. Instrum.*, vol. 83, no. 12, p. 125001, Dec. 2012, doi: 10.1063/1.4769050.

[31] X. Zheng *et al.*, “Ultralight, ultrastiff mechanical metamaterials,” *Science*, vol. 344, no. 6190, pp. 1373–1377, Jun. 2014, doi: 10.1126/science.1252291.

[32] P. F. Jacobs, “Fundamentals of Stereolithography,” p. 16.

[33] M. Aliabouzar, G. L. Zhang, and K. Sarkar, “Acoustic and mechanical characterization of 3D-printed scaffolds for tissue engineering applications,” *Biomed. Mater.*, vol. 13, no. 5, p. 055013, Aug. 2018, doi: 10.1088/1748-605X/aad417.

[34] D. Behera *et al.*, “Current challenges and potential directions towards precision microscale additive manufacturing – Part IV: Future perspectives,” *Precis. Eng.*, vol. 68, pp. 197–205, Mar. 2021, doi: 10.1016/j.precisioneng.2020.12.014.

[35] New Pro 3D, “Effects of print window material on separation force of 3d printed objects in DLP SLA printing processes,” *NewPro3-Forcast Reseearch Dev. Corp*, p. 8, May 2018.

[36] L. D. LANDAU and E. M. LIFSHITZ, “CHAPTER II - VISCOUS FLUIDS,” in *Fluid Mechanics (Second Edition)*, L. D. LANDAU and E. M. LIFSHITZ, Eds. Pergamon, 1987, pp. 44–94.

[37] C. Zhou, Y. Chen, Z. Yang, and B. Khoshnevis, “Digital material fabrication using mask-image-projection-based stereolithography,” *Rapid Prototyp. J.*, vol. 19, no. 3, pp. 153–165, Apr. 2013, doi: 10.1108/13552541311312148.

[38] P. Kunwar, Z. Xiong, S. T. Mcloughlin, and P. Soman, “Oxygen-Permeable Films for Continuous Additive, Subtractive, and Hybrid Additive/Subtractive Manufacturing,” *3D Print. Addit. Manuf.*, vol. 7, no. 5, pp. 216–221, Oct. 2020, doi: 10.1089/3dp.2019.0166.

[39] D. Yao *et al.*, “Achieving the Upper Bound of Piezoelectric Response in Tunable, Wearable 3D Printed Nanocomposites,” *Adv Funct Mater*, p. 11, 2019.

[40] X. Song, “SLURRY BASED STEREOLITHOGRAPHY: A SOLID FREEFORM FABRICATION METHOD OF CERAMICS AND COMPOSITES,” *Univ. South. Calif.*, p. 174, Aug. 2016.

[41] S. P. Gentry and J. W. Halloran, “Depth and width of cured lines in photopolymerizable ceramic suspensions,” *J. Eur. Ceram. Soc.*, vol. 33, no. 10, pp. 1981–1988, Sep. 2013, doi: 10.1016/j.jeurceramsoc.2013.02.033.

[42] Y. Chen, “PZT ceramics fabricated based on stereolithography for an ultrasound transducer array application,” *Ceram. Int.*, p. 6, 2018.

[43] A. Smirnov, S. Chugunov, A. Kholodkova, M. Isachenkov, A. Vasin, and I. Shishkovsky, “Progress and challenges of 3D-printing technologies in the manufacturing of piezoceramics,” *Ceram. Int.*, vol. 47, no. 8, pp. 10478–10511, Apr. 2021, doi: 10.1016/j.ceramint.2020.12.243.

[44] T. Chartier, C. Hinczewski, and S. Corbel, “UV Curable Systems for Tape Casting,” *J. Eur. Ceram. Soc.*, vol. 19, no. 1, pp. 67–74, Jan. 1999, doi: 10.1016/S0955-2219(98)00177-0.

[45] Z. Chen *et al.*, “3D printing of piezoelectric element for energy focusing and ultrasonic sensing,” *Nano Energy*, vol. 27, pp. 78–86, Sep. 2016, doi: 10.1016/j.nanoen.2016.06.048.

[46] R. M. German, P. Suri, and S. J. Park, “Review: liquid phase sintering,” *J. Mater. Sci.*, vol. 44, no. 1, pp. 1–39, Jan. 2009, doi: 10.1007/s10853-008-3008-0.

[47] D. Wang, H. Guo, C. S. Morandi, C. A. Randall, and S. Trolier-McKinstry, “Cold sintering and electrical characterization of lead zirconate titanate piezoelectric ceramics,” *APL Mater.*, vol. 6, no. 1, p. 016101, Jan. 2018, doi: 10.1063/1.5004420.

[48] L. Yang, O. Harrysson, H. West, and D. Cormier, “Mechanical properties of 3D re-entrant honeycomb auxetic structures realized via additive manufacturing,” *Int. J. Solids Struct.*, vol. 69–70, pp. 475–490, Sep. 2015, doi: 10.1016/j.ijsolstr.2015.05.005.

[49] S. Marselli, V. Pavia, C. Galassi, E. Roncari, F. Craciun, and G. Guidarelli, “Porous piezoelectric ceramic hydrophone,” p. 7.

[50] L. J. Gibson and M. F. Ashby, *Cellular Solids: Structure and Properties*, 2nd ed. Cambridge: Cambridge University Press, 1997.

[51] M. F. Ashby, “The properties of foams and lattices,” *Philos. Trans. R. Soc. Math. Phys. Eng. Sci.*, vol. 364, no. 1838, pp. 15–30, Jan. 2006, doi: 10.1098/rsta.2005.1678.

[52] L. Bai, C. Yi, X. Chen, Y. Sun, and J. Zhang, “Effective Design of the Graded Strut of BCC Lattice Structure for Improving Mechanical Properties,” *Materials*, vol. 12, no. 13, p. 2192, Jul. 2019, doi: 10.3390/ma12132192.

[53] W. A. Smith and B. A. Auld, “Modeling 1-3 composite piezoelectrics: thickness-mode oscillations,” *IEEE Trans. Ultrason. Ferroelectr. Freq. Control*, vol. 38, no. 1, pp. 40–47, Jan. 1991, doi: 10.1109/58.67833.

[54] W. A. Smith, “Modeling 1-3 composite piezoelectrics: hydrostatic response,” *IEEE Trans. Ultrason. Ferroelectr. Freq. Control*, vol. 40, no. 1, pp. 41–49, Jan. 1993, doi: 10.1109/58.184997.

[55] R. Gentilman *et al.*, “SonoPanel 1-3 piezocomposite hydrophone-actuator panels,” in *“Challenges of Our Changing Global Environment”. Conference Proceedings. OCEANS ’95 MTS/IEEE*, San Diego, CA, USA, 1995, vol. 3, pp. 2032–2037, doi: 10.1109/OCEANS.1995.528890.

[56] J. M. Cannata, J. A. Williams, Qifa Zhou, T. A. Ritter, and K. K. Shung, “Development of a 35-MHz piezo-composite ultrasound array for medical imaging,” *IEEE Trans. Ultrason. Ferroelectr. Freq. Control*, vol. 53, no. 1, pp. 224–236, Jan. 2006, doi: 10.1109/TUFFC.2006.1588408.

[57] E. K. Akdogan, M. Allahverdi, and A. Safari, “Piezoelectric composites for sensor and actuator applications,” *IEEE Trans. Ultrason. Ferroelectr. Freq. Control*, vol. 52, no. 5, pp. 746–775, May 2005, doi: 10.1109/TUFFC.2005.1503962.

[58] V. T. Rathod, “A Review of Acoustic Impedance Matching Techniques for Piezoelectric Sensors and Transducers,” *Sensors*, vol. 20, no. 14, p. 4051, Jul. 2020, doi: 10.3390/s20144051.

[59] E. Dong *et al.*, “Bioinspired metagel with broadband tunable impedance matching,” *Sci. Adv.*, vol. 6, no. 44, p. eabb3641, Oct. 2020, doi: 10.1126/sciadv.abb3641.

[60] B. Wojciechowski, K. Wetter, C. Cheepa, T. Sample, and B. Sharma, “Acoustic Properties of 3D Printed Bulk Absorbers with Novel Surface Topologies,” p. 20.

[61] S. Herold and D. Mayer, “Adaptive Piezoelectric Absorber for Active Vibration Control,” *Actuators*, vol. 5, no. 1, p. 7, Feb. 2016, doi: 10.3390/act5010007.

[62] G. Yang, L. Dai, G. Si, S. Wang, and S. Wang, “Challenges and Security Issues in Underwater Wireless Sensor Networks,” *Procedia Comput. Sci.*, vol. 147, pp. 210–216, 2019, doi: 10.1016/j.procs.2019.01.225.

[63] S. Sadeghpour, S. Meyers, J.-P. Kruth, J. Vleugels, M. Kraft, and R. Puers, “Resonating Shell: A Spherical-Omnidirectional Ultrasound Transducer for Underwater Sensor Networks,” *Sensors*, vol. 19, no. 4, p. 757, Feb. 2019, doi: 10.3390/s19040757.

[64] I. F. Akyildiz, D. Pompili, and T. Melodia, “Underwater acoustic sensor networks: research challenges,” *Ad Hoc Netw.*, vol. 3, no. 3, pp. 257–279, May 2005, doi: 10.1016/j.adhoc.2005.01.004.

[65] I. T. Jones, J. A. Stanley, J. Bonnel, and T. A. Mooney, “Complexities of tank acoustics warrant direct, careful measurement of particle motion and pressure for bioacoustic studies,” Bruges, Belgium, 2019, p. 010005, doi: 10.1121/2.0001073.

[66] G. D. Hugus, “An Analysis of the Effect of Vibration Sensitivity on Hydrophone Design,” p. 44.

[67] W. M. Carey, J. D. Holmes, and J. F. Lynch, “The applicability of a small autonomous vehicle towed array system to ocean acoustic measurements and signal processing,” Paris, France, 2008, pp. 070007–070007, doi: 10.1121/1.3196623.

[68] S. Jiménez-Gambín, N. Jiménez, J. M. Benlloch, and F. Camarena, “Holograms to focus arbitrary ultrasonic fields through the skull,” *Phys. Rev. Appl.*, vol. 12, no. 1, p. 014016, Jul. 2019, doi: 10.1103/PhysRevApplied.12.014016.

[69] P. Kruizinga *et al.*, “Compressive 3D ultrasound imaging using a single sensor,” *Sci. Adv.*, vol. 3, no. 12, p. e1701423, Dec. 2017, doi: 10.1126/sciadv.1701423.

[70] J.-Y. Chapelon *et al.*, “New piezoelectric transducers for therapeutic ultrasound,” *Ultrasound Med. Biol.*, vol. 26, no. 1, pp. 153–159, Jan. 2000, doi: 10.1016/S0301-5629(99)00120-9.

[71] P. X. Tran, “A Study of Measuring Intracranial Pressure Using a Non-Invasive Piezoelectric Sensor.” Virginia Tech, Oct. 29, 2014.

[72] C. Wang *et al.*, “Monitoring of the central blood pressure waveform via a conformal ultrasonic device,” *Nat. Biomed. Eng.*, vol. 2, no. 9, pp. 687–695, Sep. 2018, doi: 10.1038/s41551-018-0287-x.

[73] H. Hu *et al.*, “Stretchable ultrasonic transducer arrays for three-dimensional imaging on complex surfaces,” *Sci. Adv.*, p. 12, 2018.

[74] A. Bhargava and S. Shahab, “Acoustic-electroelastic modeling of piezoelectric disks in high-intensity focused ultrasound power transfer systems,” *J. Intell. Mater. Syst. Struct.*, p. 1045389X2097547, Dec. 2020, doi: 10.1177/1045389X20975478.

[75] B. D. M. Chaparro-Rico, F. Sebastiano, and D. Cafolla, “A Smart Stent for Monitoring Eventual Restenosis: Computational Fluid Dynamic and Finite Element Analysis in Descending Thoracic Aorta,” *Machines*, vol. 8, no. 4, p. 81, Nov. 2020, doi: 10.3390/machines8040081.

[76] K. M. Awan, P. A. Shah, K. Iqbal, S. Gillani, W. Ahmad, and Y. Nam, “Underwater Wireless Sensor Networks: A Review of Recent Issues and Challenges,” *Wirel. Commun. Mob. Comput.*, vol. 2019, pp. 1–20, Jan. 2019, doi: 10.1155/2019/6470359.

[77] A. Ahmed and M. Younis, “Acoustic Beam Characterization and Selection for Optimized Underwater Communication,” *Appl. Sci.*, vol. 9, no. 13, p. 2740, Jul. 2019, doi: 10.3390/app9132740.

[78] Y. Kim, A. D. Maxwell, T. L. Hall, Z. Xu, K.-W. Lin, and C. A. Cain, “Rapid prototyping fabrication of focused ultrasound transducers,” *IEEE Trans. Ultrason. Ferroelectr. Freq. Control*, vol. 61, no. 9, pp. 1559–1574, Sep. 2014, doi: 10.1109/TUFFC.2014.3070.

[79] M. L. Lifson, M.-W. Kim, J. R. Greer, and B.-J. Kim, “Enabling Simultaneous Extreme Ultra Low- *k* in Stiff, Resilient, and Thermally Stable Nano-Architected Materials,” *Nano Lett.*, vol. 17, no. 12, pp. 7737–7743, Dec. 2017, doi: 10.1021/acs.nanolett.7b03941.

[80] R. Madrak and M. Popovic, “Dielectric Constant of Castor Oil,” p. 17.

[81] R. Hooke 1635-1703., D. Papin 1647-1714., James. Young, S. Sturmy 1633-1669., and G. T., *Lectures de potentia restitutiva, or, Of spring explaining the power of springing bodies : to which are added some collections viz. a description of Dr. Pappins wind-fountain and force-pump, Mr. Young’s observation concerning natural fountains, some other considerations concerning that subject, Captain Sturmy’s remarks of a subterraneous cave and cistern, Mr. G.T. observations made on the Pike of Teneriff, 1674, some reflections and conjectures occasioned thereupon, a relation of a late eruption in the Isle of Palma*. London : Printed for John Martyn ..., 1678.

[82] S. Houghtaling, “Air-gap hydrophone,” *J. Acoust. Soc. Am.*, vol. 94, no. 4, pp. 2466–2467, Oct. 1993, doi: 10.1121/1.407428.

[83] D. Chen, “A Multi-Material Projection Stereolithography System for Manufacturing Programmable Negative Poisson’s Ratio Structures.” Virginia Tech Department of Mechnanical Engineering, Dec. 12, 2016.

[84] X. Song, Y. Chen, T. W. Lee, S. Wu, and L. Cheng, “Ceramic fabrication using Mask-Image-Projection-based Stereolithography integrated with tape-casting,” *J. Manuf. Process.*, vol. 20, pp. 456–464, Oct. 2015, doi: 10.1016/j.jmapro.2015.06.022.

[85] A. J. Duncan, K. Lucke, C. Erbe, and R. D. McCauley, “Issues associated with sound exposure experiments in tanks,” Dublin, Ireland, 2016, p. 070008, doi: 10.1121/2.0000280.

[86] G. Allen, “Field-Driven Design.” nTopology, 2020.

[87] A. Salado, “A systems-theoretic articulation of stakeholder needs and system requirements,” *Syst. Eng.*, vol. 24, no. 2, pp. 83–99, Mar. 2021, doi: 10.1002/sys.21568.

[88] Waymo LLC, Ed., “Waymo Driver,” Waymo, 2021. [Online]. Available: https://waymo.com/waymo-driver/. [Accessed: 07-May-2021].